iScience

CellPress
OPEN ACCESS

Article

Redox modulator iron complexes trigger intrinsic apoptosis pathway in cancer cells

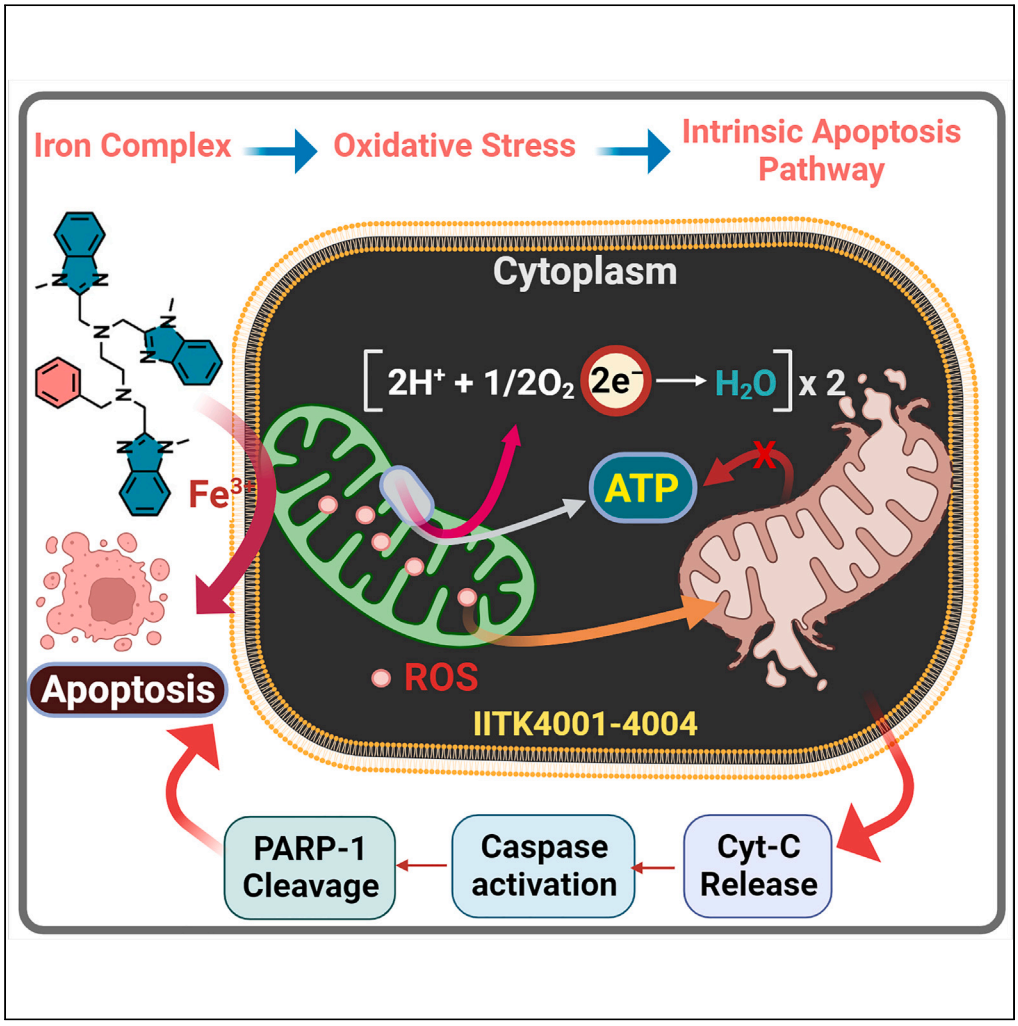

Sai Kumari Vechalapu, Rakesh Kumar, Niranjan Chatterjee, ..., Santosh K. Misra, Apparao Draksharapu, Dharmaraja Allimuthu

skmisra@iitk.ac.in, appud@iitk.ac.in, atdharma@iitk.ac.in

Highlights

Cancer's drug resistance spurs need for new therapies

Iron chelators halt liver cancer growth via redox disruption

Iron complexes induce oxidative stress, triggering apoptosis

Exploiting iron overload, a unique anticancer strategy

Vechalapu et al., iScience 27, 109899
June 21, 2024
https://doi.org/10.1016/j.isci.2024.109899

iScience

CellPress
OPEN ACCESS

Article

Redox modulator iron complexes trigger intrinsic apoptosis pathway in cancer cells

Sai Kumari Vechalapu,[1] Rakesh Kumar,[1] Niranjan Chatterjee,[2] Sikha Gupta,[1] Shweta Khanna,[1] Pooja Yedehalli Thimmappa,[3] Sathyapriya Senthil,[1] Raju Eerlapally,[1] Manjunath B. Joshi,[3] Santosh K. Misra,[2,*] Apparao Draksharapu,[1,*] and Dharmaraja Allimuthu[1,4,*]

SUMMARY

The emergence of multidrug resistance in cancer cells necessitates the development of new therapeutic modalities. One way cancer cells orchestrate energy metabolism and redox homeostasis is through overloaded iron pools directed by iron regulatory proteins, including transferrin. Here, we demonstrate that targeting redox homeostasis using nitrogen-based heterocyclic iron chelators and their iron complexes efficiently prevents the proliferation of liver cancer cells (EC_{50}: 340 nM for IITK4003) and liver cancer 3D spheroids. These iron complexes generate highly reactive Fe(IV)=O species and accumulate lipid peroxides to promote oxidative stress in cells that impair mitochondrial function. Subsequent leakage of mitochondrial cytochrome c activates the caspase cascade to trigger the intrinsic apoptosis pathway in cancer cells. This strategy could be applied to leverage the inherent iron overload in cancer cells to selectively promote intrinsic cellular apoptosis for the development of unique iron-complex-based anticancer therapeutics.

INTRODUCTION

Cancer is the leading source of deaths worldwide, and the emergence of drug resistance to the existing class of anticancer therapeutics warrants novel therapeutic interventions. While organic small molecule therapeutics continue to dominate the medicinal chemistry, milestone therapeutic cisplatin is crowned as the major metal-based therapeutic to rule cancer therapy for the past four decades.[1] Apart from cisplatin,[1] carboplatin and oxaliplatin are the follow-up platinum drugs widely used for treating cancer. These molecules predominantly function through the plastination of DNA (deoxyribonucleic acid) by intrastrand cross-linking of deoxyguanosine residues in cells among several other mechanisms.[2] Metal-based therapeutics that operate beyond DNA targeting mechanisms in cancer cells could serve as potential alternatives to strengthen the arsenal of metal-based anticancer drugs.[3–12] Beyond cisplatin- or platinum-based anticancer drugs, several gold- and ruthenium-based cancer therapeutics are in the clinical trials. Several iron complexes including iron-ferrocene and imine complexes exhibit submicromolar potency and function through the induction of reactive oxygen species (ROS) in cancer cells for their mechanism of action.[13–16] These compounds represent a novel avenue for therapeutic development in oncology, offering diverse mechanisms for targeting malignant cells.

Metal ion homeostasis is essential for cell signaling, growth, survival, and metabolism.[17] Particularly, systemic functions and metabolism of iron are regulated by ferroportin and iron-regulatory proteins.[17] Transferrin, iron-responsive element-binding proteins (IRPs), and iron-sulfur cluster proteins (ISCs) transfer and regulate iron homeostasis in cells, which are critical for oxygen transport, respiration, cell signaling, proliferation, and metabolism.[18] However, the accumulation of free iron and disruption of its homeostasis is recorded in several cancers and other diseases.[17,19,20] The ROS-generating capability of free iron pools, leading to DNA damage and mutations, is well characterized as a responsible factor for cancer onset and progression.[21] In parallel, a high level of iron is essential for balancing the fast metabolism and respiration in cancer cells, for example, bone and liver cancer cells are known to possess high iron content than their respective normal cells.[21–24] Trapping intracellular metal ions using organic ligands has proved successful in eliminating the tumor.[25–27] Instead of oxidative phosphorylation in mitochondria, cancer cells depend on aerobic glycolysis for energy production called "Warburg effect," an ineffective process to produce ATP.[28] Therefore, a disruption of this oxidative metabolism by depleting intracellular iron would make the cancer cells vulnerable to iron chelators. We hypothesized to additionally challenge the cancer cell survival by turning its intracellular iron into an iron complex capable of generating deleterious ROS that could promote oxidative cell death. Here, we report the identification of iron complexes and their ligands, nitrogen-based heterocyclic scaffolds chelating with iron, that oxidatively impair mitochondrial function to trigger intrinsic apoptosis pathway in cancer cells.

[1]Department of Chemistry, Indian Institute of Technology Kanpur, Uttar Pradesh 208016, India
[2]Department of Biological Sciences and Bioengineering, Indian Institute of Technology Kanpur, Uttar Pradesh 208016, India
[3]Department of Ageing Research, Manipal School of Life Sciences, Manipal Academy of Higher Education, Manipal 576104, India
[4]Lead contact
*Correspondence: skmisra@iitk.ac.in, appud@iitk.ac.in, atdharma@iitk.ac.in
https://doi.org/10.1016/j.isci.2024.109899

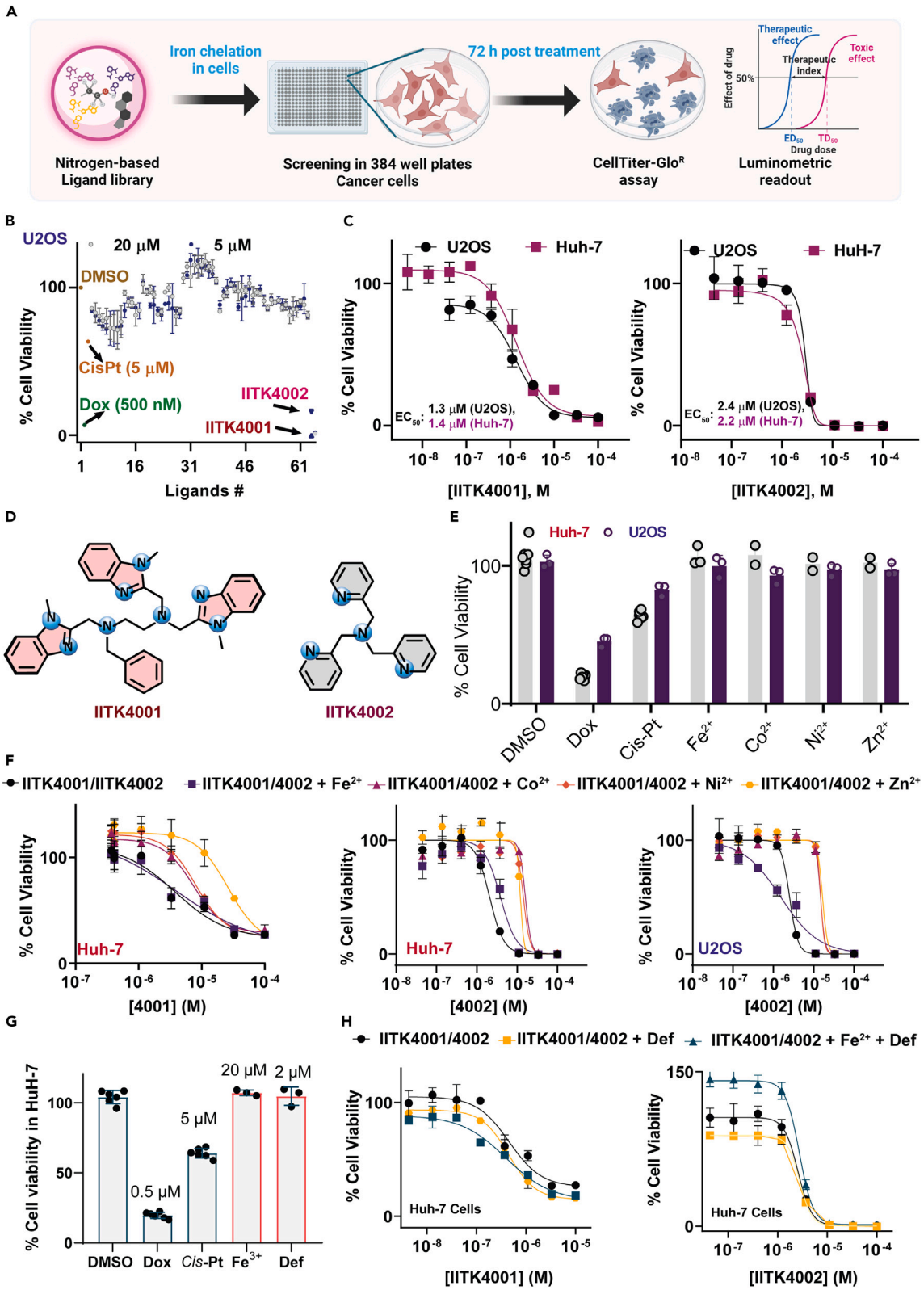
A
Iron chelation in cells
72 h post treatment
Therapeutic effect
Toxic effect
Therapeutic index
Effect of drug
50%
ED50
TD50
Drug dose
Nitrogen-based Ligand library
Screening in 384 well plates Cancer cells
CellTiter-Glo® assay
Luminometric readout
B
U2OS
20 µM
5 µM
DMSO
CisPt (5 µM)
Dox (500 nM)
IITK4002
IITK4001
% Cell Viability
Ligands #
C
U2OS
Huh-7
HuH-7
EC50: 1.3 µM (U2OS), 1.4 µM (Huh-7)
EC50: 2.4 µM (U2OS), 2.2 µM (Huh-7)
[IITK4001], M
[IITK4002], M
D
IITK4001
IITK4002
E
Huh-7
U2OS
DMSO
Dox
Cis-Pt
F
IITK4001/IITK4002
IITK4001/4002 + Fe2+
IITK4001/4002 + Co2+
IITK4001/4002 + Ni2+
IITK4001/4002 + Zn2+
[4001] (M)
[4002] (M)
G
% Cell viability in HuH-7
20 µM
2 µM
5 µM
0.5 µM
DMSO
Dox
Cis-Pt
Fe3+
Def
H
IITK4001/4002
IITK4001/4002 + Def
IITK4001/4002 + Fe2+ + Def
Huh-7 Cells
[IITK4001] (M)
[IITK4002] (M)

Figure 1. IITK4001 and IITK4002 promote antiproliferative activity against Huh-7 and U2OS cells with iron salt

(A) Schematic flow of ligand screening in a cell viability assay using a luminescence-based Celltiter-Glo assay after 72 h of treatment.

(B, C, E, F) Cell viability data: screening of ligand library (#75) at 20 and 5 μM (only screened in U2OS cells) (B), dose-dependent analysis of IITK4001 and IITK4002(U2OS and Huh-7) (C), treatment of metal salts alone (20 μM, Huh-7 and U2OS cells (E), and metal salts in combination with IITK4001 (Huh-7 cells) or IITK4002 (Huh-7 and U2OS cells) (F).

(D) Structures of lead ligand scaffolds IITK4001 and IITK4002.

(G and H) Antiproliferative activity of IITK4001/4002 in combination with deferoxamine (Def) and iron salt in Huh-7 cells. All graphs indicate mean ± SD. Data presented are performed in two independent cell lines and are representative of more than two independent experiments with a minimum of three technical replicates. Cell viability data are normalized relative to DMSO treatment control as 100%.

RESULTS

IITK4001 and IITK4002 traps iron and complexes to prevent cancer cell proliferation

We first synthesized ligand scaffolds (di-, tri-, tetra-, and pentadentate) on one condition that they are not planar but possess versatile three-dimensional orientations to resist DNA intercalation. Our screening of a ligand library (75 scaffolds, 20 and 5 μM) identified two hit molecules—*N*′-benzyl-*N*′,*N*′′-(tris-N-methylbenzimidazole)-ethylenediamine, IITK4001 and tris(2-pyridylmethyl)amine, IITK4002—as a potent inhibitors of osteosarcoma (U2OS) cell proliferation (Figures 1A and 1B). Both IITK4001 and IITK4002 dose-dependently inhibited the proliferation of hepatocellular carcinoma (Huh-7) and U2OS cell growth with a range of 1–2 μM EC_{50} (Figures 1C and 1D). These are nitrogen-based heterocyclic molecules, capable of acting as chelators for various metal ions[29]; therefore, we determined to investigate the role of metal complexation with 3d metals (iron, cobalt, nickel, and zinc) in the antiproliferative activity of IITK4001 and IITK4002. Hence, we treated the cells with our lead molecules alone or in combination with indicated metal salts at non-toxic concentrations (20 μM; Figure 1E). Interestingly, iron salts cotreatment with both IITK4001/IITK4002 retained or had minimal effect on the antiproliferative potential. However, other metal salts were found to suppress the activity of ligands IITK4001/IITK4002 when combined (Figure 1F). Next, to investigate whether iron depletion using our metal ion chelators in cells alone is sufficient to prevent cancer cell proliferation, we performed combination experiments with deferoxamine (Def, an iron chelator; Figures 1G and S13) at the non-toxic concentration (2 μM). We observed no substantial change in the cell survival in combination when compared to the lone treatment conditions. Yet, the addition of excess iron salt to IITK4001/4002 or in combination with Def did not rescue the cell death (Figure 1H). Therefore, we concluded the causative agent of cell death is unlikely to be iron depletion alone, rather a shift in the free iron pool to form a complex of IITK4001/4002 and a possibility of additional roles for these iron complexes in the antiproliferative activity anticipated.

Reversible cross-complexation studies of IITK4002 with Fe^{2+} and other biologically relevant metal ions

The initial examination of IITK4001 and IITK4002 led to the conclusion of iron complex formation rather than iron depletion as the dominant mechanism for preventing cancer cell proliferation. However, other metal ions in the biological system could potentially interfere with the activity. Therefore, we assembled salts of various metal ions around their physiological concentrations including alkali metals, 5 mM solution of sodium, magnesium, potassium, calcium salts, and d-block transition metals such as manganese (1 μM), iron (20 μM), cobalt (0.5 μM), nickel (0.5 μM), copper (5 μM), and zinc (100 μM) salts (Figure 2).[26] Due to the solubility issues with IITK4001 under physiological conditions, we restricted all our cross-complex formation studies with IITK4002 (Figure 2). Initially, we monitored the Fe(II)-IITK4002 formation with 0.2–2.0 equiv. of IITK4002 using UV-visible spectroscopy by following a distinct absorption at 395 nm (Figures 2A–2C). We find an instant complex formation upon the addition of Fe^{2+} to IITK4002, and this was found to be saturated with 1:1 stoichiometry, indicating the 1 to 1 complex formation. This complex was found to be irreversible and stable in the complexation medium for more than an hour (Figures 2A and 2B). To study the interference of assembled biologically relevant metal ions, an excess of these metal salts (5 equiv.) was added to the preformed Fe(II)-IITK4002 complex and monitored the change in absorbance at 395 nm. We noted no effect with any of the alkali metal ions and also with transition metal ions such as Mn^{2+}, Ni^{2+}, and Co^{2+} salts, indicating Fe(II)-IITK4002 complex is irreversible under these conditions (Figures 2D and 2E). However, we find a slow equilibration of Fe(II)-IITK4002 with Zn^{2+} over 60 min to a ~50% Fe(II)-IITK4002 (Figure 2F). Conversely, the reverse addition of Fe^{2+} salt to preformed Zn(II)-IITK4002 exhibited a rapid displacement of Zn^{2+} within a few seconds ($t_{½}$ = 4 s) to form Fe(II)-IITK4002 and observed a slow equilibration over 60 min (Figure 2G), thereby suggesting the complex is competitively reversible. Identical to this, the addition of Cu^{2+} was found to react instantly with Fe(II)-IITK4002 that in less than 20 s all the Fe(II)-IITK4002 converted into Cu(II)-IITK4002 ($t_{½}$ = 8.3 s; Figures 2H and 2I) and was found to equilibrate to nearly 50% in 6 min. Likewise, the reverse addition also exhibited a similar trend of instant conversion of Cu(II)-IITK4002 to Fe(II)-IITK4002 transformation ($t_{½}$ = 3.2 s; Figure 2J). Together, the cross-complexation studies with biologically relevant metal ions indicate that Fe(II)-IITK4002 remain unaffected with other metal ions tested, and Zn^{2+} and Cu^{2+} could potentially interfere. While the physiological concentration of copper (0.5 μM) is 4-fold lesser than iron concentration (20 μM), zinc (100 μM) level is found to be 5-fold higher than iron. Despite higher levels of Zn^{2+} in the biological systems, we have observed addition of Zn^{2+} to IITK4001 showed more of a preventive role than retaining or enhancing the cell death induced by IITK4002 (Figure 1F). The abovementioned set of experiments have clearly ruled out the majority of the biologically relevant metal ions except for a competition between Fe^{2+} and Cu^{2+}. Therefore, evaluating the individual effects of Fe^{2+} and Cu^{2+} ions on IITK4002 is essential to precisely capture the metal ion responsible for the antiproliferative activity of our lead ligand molecules.

Synthesis and physio-chemical evaluation of iron complexes (IITK4003 and IITK4004) and other 3d-metal complexes

Iron and copper are indispensable elements for redox homeostasis in cells due to their versatile redox capacity to switch between multiple oxidation states.[5,25–27,30–33] Next, we set out to investigate whether the effect of our ligands is due to their complexation with Fe^{2+} or Cu^{2+}. To

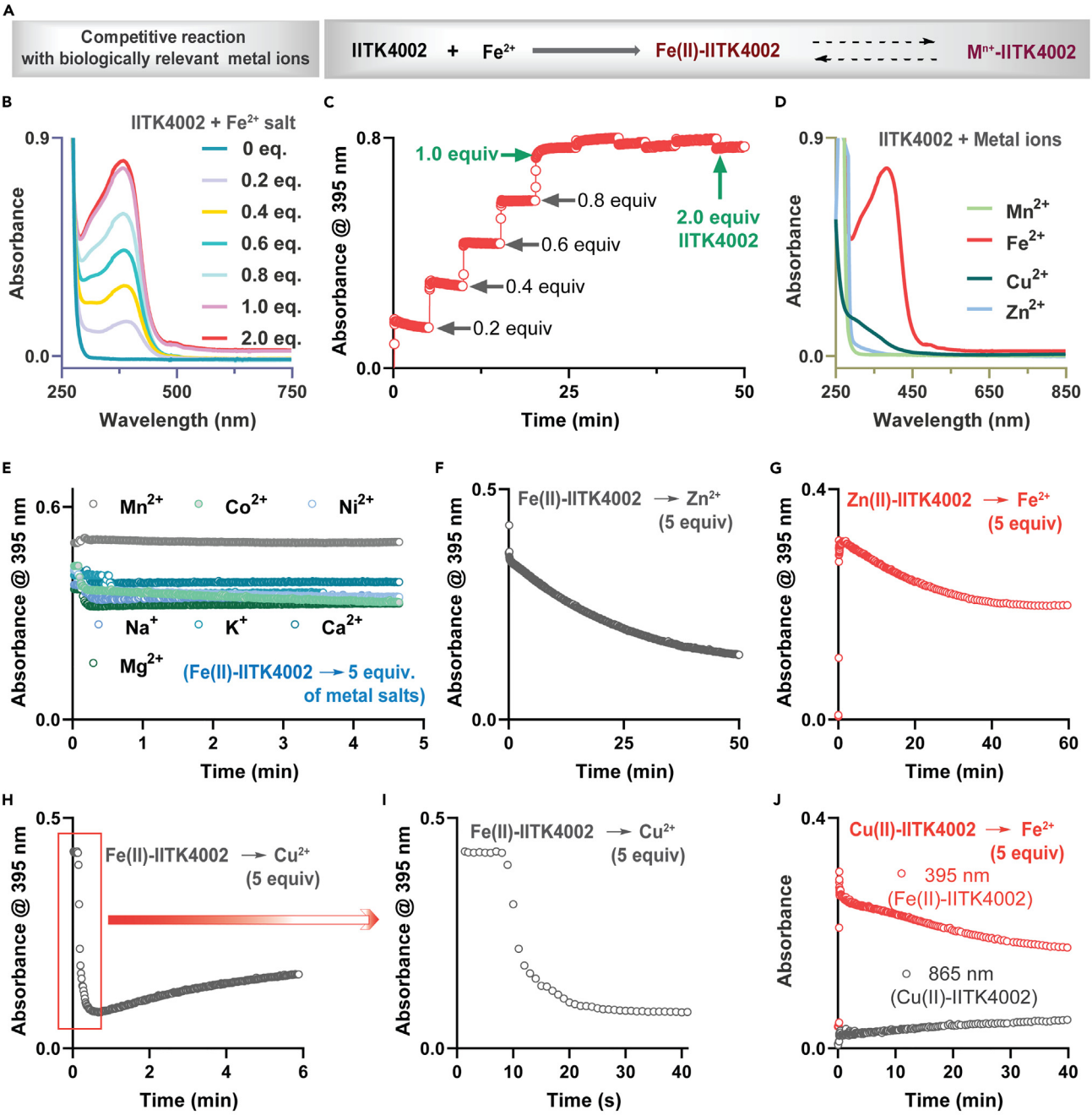

Figure 2. Fe(II)-IITK4002 is competitively reversible with Zn^{2+} and Cu^{2+} salts

(A) Scheme for competitive complexation studies for IITK4002 with Fe^{2+} and other metal ions.

(B–D) UV-visible spectra of IITK4002 with Fe^{2+} salt ($[FeII(H_2O)_6](ClO_4)_2$ (0 to 2.0 equiv.; B and C) and other metal salts (1 equiv., D) in 1:1 acetonitrile: water at RT.

(E, F, H, I) Absorbance was recorded at 395 nm for Fe(II)-IITK4002 after exposing it to indicated metal salts (5 equiv.) at RT. Metal salts: ZnII(OTf)2, $CuII(H_2O)_6(ClO_4)_2$, $CoII(H_2O)_6(ClO_4)_2$, $NiII(H_2O)_6(ClO_4)_2$, $MnII(H_2O)_6(ClO_4)_2$, NaCl, KCl, $CaCl_2$, and $MgSO_4$.

(G and J) Zn(II)-IITK4002 (g) or Cu(II)-IITK4002 (j) complex exposed to Fe^{2+} salt (5 equiv.) at RT and absorbance recorded at 395 nm for the Fe(II)-complex formation.

unambiguously characterize this, we synthesized the iron complexes IITK4003 and IITK4004 and characterized them by various spectroscopic techniques and X-ray crystallography studies (Figures 3 and S1–S5; Scheme S1, S2, Table S1).[33–35] Iron complexes IITK4003 and IITK4004 were found to show comparable growth inhibition activity against both Huh-7 and U2OS cells as in the ligands treatment alone (Figures 3A and 3B). Remarkably, IITK4003 exhibited an exceptional antiproliferative activity with an EC_{50} of 340 nM against Huh-7 cells, a 3-fold better than the

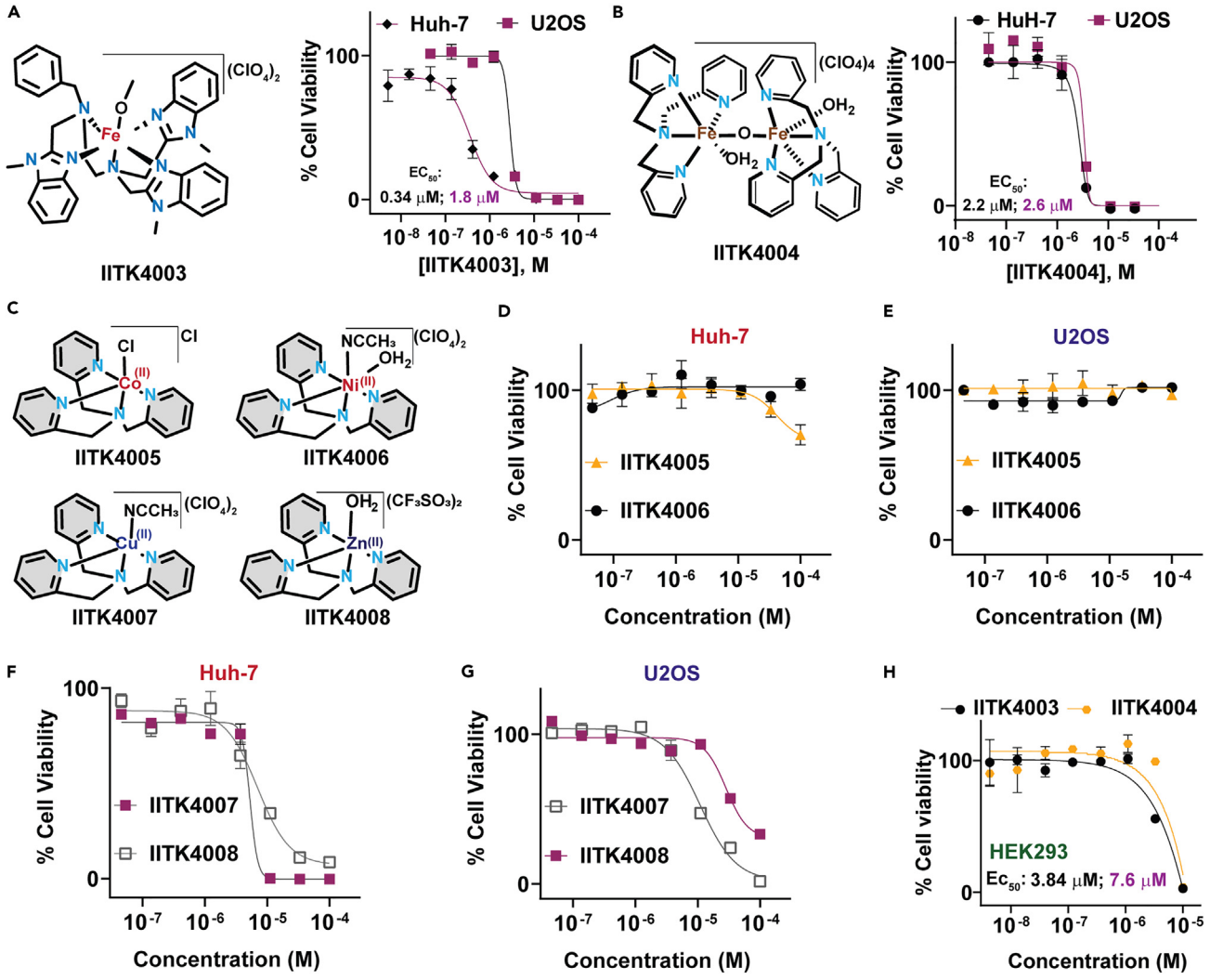

Figure 3. Iron complexes (IITK4003/4004) exhibit potent antiproliferative activity over other metal complexes in Huh-7 cells

(A–G) Cell viability of Huh-7 and U2OS cells assessed when treated with IITK4003 (A), IITK4004 (B), and IITK4005-4008 (D–G) using Celltiter-Glo assay and the structure of metal complexes studied here are given (A–C).

(H) The toxicity of lead complexes, IITK4003/4004, to HEK293 cells was assessed in a dose-dependent fashion. Graphs A, B, D–H indicate mean ± SD. Data presented are performed in two independent cell lines and are representative of more than two independent experiments with a minimum of three technical replicates. Cell viability data are normalized relative to DMSO treatment control as 100%.

parent ligand IITK4001 (Figure 3A). This difference in potency could be partially attributed to the better solubility of the complex over the ligand in aqueous conditions. Next, we synthesized authentic metal complexes of IITK4002 with other 3d-metal salts, Co^{2+} (IITK4005), Ni^{2+} (IITK4006), Cu^{2+} (IITK4007), and Zn^{2+} (IITK4008) (Figure 3C). The complexation of these 3d-metal ions with IITK4001 failed due to experimental difficulty in crystallizing and obtaining pure complexes. Then, we evaluated for their ability to prevent the growth of Huh-7 and U2OS in a dose-dependent fashion. In our evaluation for the antiproliferative activity of IITK4005 and IITK4006, both were found to be non-toxic even at 100 μM concentrations (Figures 3C–3E), suggesting Co^{2+} and Ni^{2+} complexation is unlikely to be responsible for the ligand's anti-proliferative activity. Interestingly, two of the metal ions found to be competitive in complexing with IITK4002, Cu^{2+} (IITK4007) and Zn^{2+} (IITK4008), exhibited a weak potency (5.4 μM, 7 μM in Huh-7, and 12.8 μM and >50 μM in U2OS for IITK4007 and IITK4008, respectively) in preventing the growth of cancer cells evaluated. However, the antiproliferative potencies were significantly lower than the parent ligand alone or the respective iron complex, IITK4004 (Figures 3C, 3F, and 3G). Together, the evaluation of metal complexes and the combination of various metal salts with heterocyclic ligands highlight that their antiproliferative activity arises predominantly due to iron complex formation in cells. Next, we extended the cell viability assay in the human embryonic kidney (HEK293) to estimate the selectivity index (SI) of our lead complexes (IITK4003 and IITK4004). We recorded an EC_{50} of 3.82 μM for IITK4003 with HEK293 cells, an estimated SI of 9.0 (EC_{50} in 0.34 μM), and an SI of 3.4 for Huh-7 cells (EC_{50}: 7.6 μM with HEK293 cells and 2.2 μM with Huh-7 cells, Figure 3H). Overall, IITK4003/4004 showed better

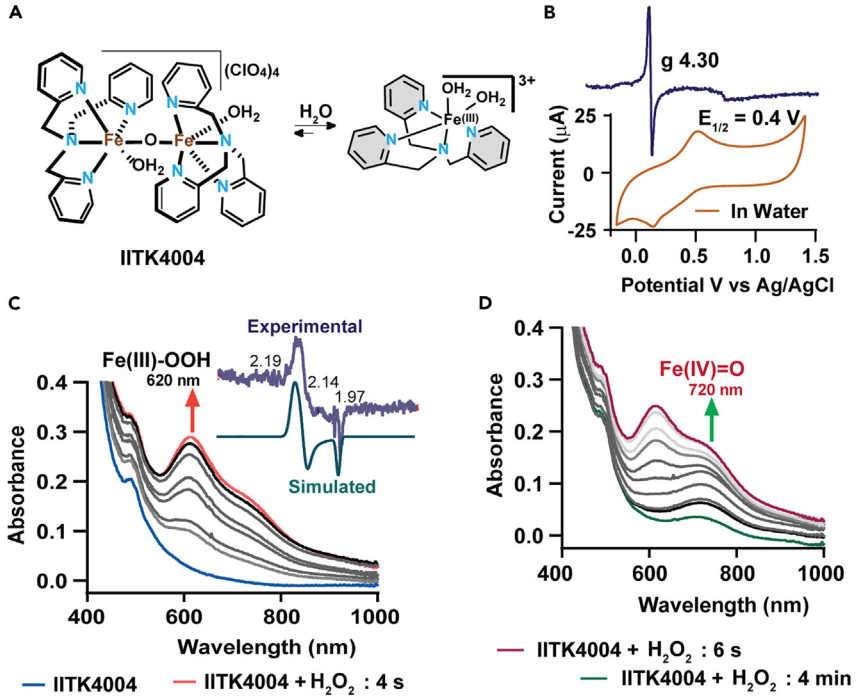

Figure 4. Iron complex, IITK4004, generates reactive metal-oxo species under simulated physiological conditions

(A and B) Monomerization of IITK4004 in water assessed using X-band EPR spectrum of IITK4004 in water/CH3CN at 120 K (insert) and cyclic voltammogram in water.

(C) UV/Vis absorption spectral studies depicting reactive meta-oxo species formation ([(TPA)Fe(III)-OOH]2+ (620 nm) and its X-band EPR spectrum compared with simulated EPR spectrum (insert).

(D) The transformation of $[(TPA)(III)Fe\text{-}OOH]^{2+}$ (620 nm) to $[(TPA)Fe(IV) = O]^{2+}$ (720 nm) in a reaction of IITK4004 with H2O2 (10 equiv.) in water is monitored using UV/Vis absorption spectral studies.

selectivity in preventing liver cancer cells' growth (Huh-7) over normal kidney cells. These studies together suggested that the complexation of iron with IITK4001/4002 is a major determinant for the antiproliferative action in Huh-7 and U2OS cells.

IITK4003/4004 generates reactive metal-oxo species under aqueous conditions

In addition to iron depletion, we anticipated a lead redox role for our top hits' mechanism of action in cells. The redox mechanisms of Fe(II) complexes would generate ROS in cells to trigger redox imbalance. The delicate balance of redox homeostasis is essential for cancer cell survival and metastasis, which could be capitalized on for developing selective cancer therapeutics.[36–38] Therefore, we evaluated the redox reactivity of IITK4004 with peroxides in water (Figures 4A–4D and S7–S11), a study thus far not investigated, majorly owing to the instability of reactive metal-oxo species in an aqueous milieu. While we expect the dinuclear iron complex IITK4004 to be electron paramagnetic resonance (EPR)-silent (due to antiferromagnetic coupling), we observed a high spin S = 5/2 signal, indicative of monomeric $[Fe(III)\text{-}IITK4002]^{3+}$ formation upon dissolution (Figures 4A, 4B, and S11).[39] Our cyclic voltammetry (CV) studies of IITK4004 and *in situ* prepared Fe(II)-IITK4002 in water exhibited a reversible redox wave at $E_{1/2}$ 0.4 V vs. Ag/AgCl, whereas $E_{1/2}$ of 1.2 V vs. Ag/AgCl in acetonitrile indicated more facile oxidation in water (Figures 4A, 4B, and S7). Next, we exposed IITK4004 in water to H_2O_2 and observed a characteristic absorption for $[(IITK4002)Fe(III)\text{-}OOH]^{2+}$ species at 620 nm, and this species was also characterized using EPR spectroscopy (g values: 2.19, 2.14, and 1.97; Figure 4C).[39–42] Together, these data indicate that IITK4004 produces a monomeric $[(IITK4002)Fe(III)\text{-}OOH]^{2+}$ species in water upon the interaction with H_2O_2. Unlike in acetonitrile (Figures S7–S11), the $[(IITK4002)Fe(III)\text{-}OOH]^{2+}$ in water converts temporally to $[(IITK4002)Fe(IV) = O]^{2+}$ with an absorption band at 720 nm (Figures 4C and 4D).[43] A similar set of reactivity patterns was observed for IITK4004 with *tert*-butyl hydroperoxide (^{t}BuOOH) to generate reactive oxidative species $[(IITK4002)Fe(IV) = O]^{2+}$(Figures S8D and S10).[44,45] Further, we independently mixed IITK4002 with Fe^{2+} and Fe^{3+} salts for *in situ* formation of (IITK4002)Fe(II) and (IITK4002)Fe(III) complexes. To our delight, exposing them to H_2O_2 and ^{t}BuOOH produced a similar Fe(III)-OOH and Fe(III)-OO^{t}Bu, respectively, which decayed to yield the highly reactive $[(IITK4002)Fe(IV) = O]^{2+}$ complex (Figures 4C, 4D, and S11). A comparable study for IITK4003 capturing metal-oxo species formation (Figure S6) has strongly suggested that both complexes possess a strong oxidative capacity with peroxides under physiological conditions.

ROS generation by IITK4001-IITK4004 accumulates lipid peroxide but no sign of DNA damage

After establishing the formation of reactive iron-oxo intermediates with peroxides under *in vitro* conditions, we assessed the cellular ROS generation with our hits. Initially, we performed the Amplex Red assay to quantify extracellular ROS upon treatment of Huh-7 cells with our lead

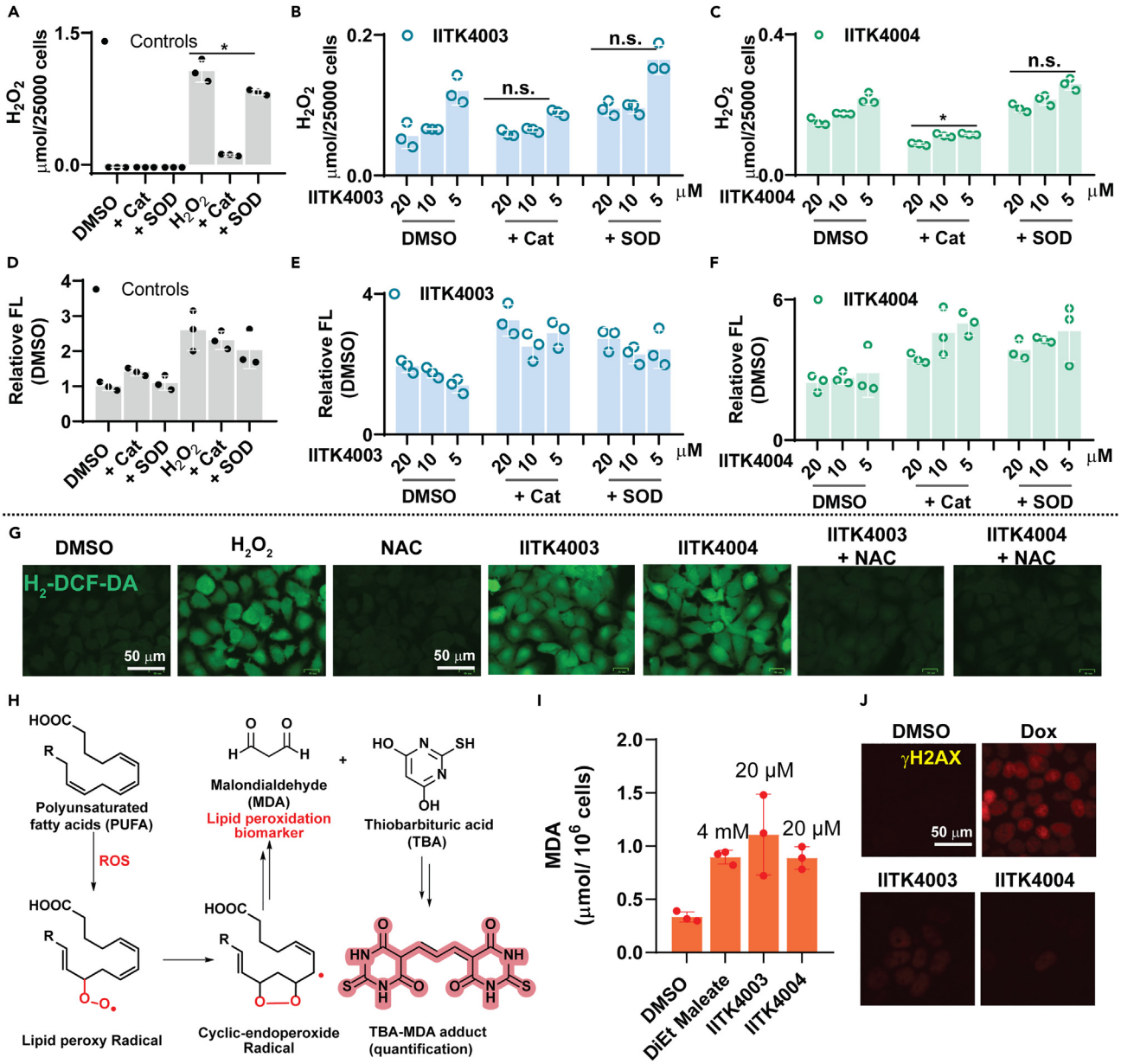

Figure 5. Lead molecules accumulate lipid peroxide to induce oxidative stress in cancer cells

(A–F) Extracellular ROS was quantified after the treatment of Huh-7 cells with IITK4003/4004 in combination with catalase and superoxide dismutase enzymes using fluorescence-based Amplex red assay (A–C) and DHE oxidation assay (D–F).

(G) Intracellular ROS accumulation was visualized using H_2-DCFDA oxidation experiment. Scale bar: 25 μm.

(H, I) Schematic depicting polyunsaturated fatty acid (PUFA, lipid) peroxidation in cells (H) and its quantification through MDA using TBARS assay (I).

(J) Immunofluorescence analysis of cells stained with anti-γH2AX upon treatment with doxorubicin (Dox) and lead molecules (20 μM). Scale bar: 25 μm. Graphs A–F and I indicate mean ± SD. Data presented are representative of more than two independent replicates and a minimum of three technical replicates.

molecules (Figures 5A–5C).[46] Indeed, our lead molecules generated ROS extracellularly and addition of catalase enzyme (a quencher of hydrogen peroxide) or superoxide dismutase enzyme (SOD, converts superoxide radical anion into hydrogen peroxide) had partial or minimal effect on the IITk4003/4004-induced ROS generation (Figures 5A–5C). We also used another fluorescence-based assay, dihydroethidine (DHE) oxidation assay for ROS measurement. The DHE reacts with superoxide radical anion to generate 2-hydroxy ethidium and hydroxy radical to generate ethidium as oxidized products.[46–48] We observed a similar trend in ROS generation as in the Amplex Red assay that our lead molecules profoundly generated ROS, whereas the ROS quenchers such as catalase or SOD exhibited no suppression of ROS levels

(Figures 5D–5F). These studies led to the conclusion that in addition to superoxide radical anion or hydrogen peroxide, the highly reactive metal-oxo species could generate other oxidized biomolecules and promote oxidative stress. Next, we assessed the intracellular ROS generation with our lead molecules alone or in combination with oxidant (H_2O_2) and antioxidant (*N*-acetylcysteine). We used a turn-on fluorescence-based H_2DCF-DA oxidation assay in Huh-7 and U2OS cells to measure the intracellular ROS accumulation. We observed a sharp increase in the fluorescence intensity with IITK4003/4004 similar to H_2O_2 treatment, suggesting the accumulation of intracellular ROS. Conversely, combining our top hits with antioxidant *N*-acetylcysteine (NAC) has rescued the ROS effect (Figures 5G and S14). Two of the most sensitive biomolecules to intracellular ROS accumulations are deoxyribonucleic acid (DNA) and lipid molecules. First, we assessed the lipid peroxidation in cells when exposed to our lead molecules. Peroxidation of polyunsaturated fatty acids (PUFA) is known to convert them into malondialdehyde (MDA), which could be trapped using condensation chemistry with thiobarbituric acid (TBA) (Figure 5H) in a TBARS (thiobarbituric acid reactive substance) assay.[49] Quantification of MDA-TBA condensed product indicated a 2- to 3-fold enhancement in the levels of lipid peroxides (Figures 5I and S15). Besides, DNA damage is a routine mechanism predicted when metal-complex-mediated ROS generation is captured.[50] However, our analysis of H2AX protein phosphorylation at gamma position, a biomarker for DNA damage mechanism (γ-H2AX), using immunofluorescence imaging, displayed minimal or no effect compared to doxorubicin (Dox, Figures 5J and S16), thereby ruling out DNA damage mechanisms responsible for antiproliferative activity. Therefore, we concluded that the cancer cell death induced by our lead molecules could potentially arise due to lipid peroxide accumulation rather than DNA-damage-mediated mechanism.

Iron complexes accumulate lipid peroxide and do not induce ferroptosis

Thus far, the results of iron complexes enhancing intracellular ROS accumulation leading to lipid peroxidation have instinctively driven us to investigate the cell death mechanism of ferroptosis, an iron-dependent oxidative cell death induced through lipid peroxide accumulation.[51] Ferroptosis has been linked with multiple steps in the biosynthesis of glutathione and its redox cycling. For example, erastin is reported to inhibit cystine uptake to induce ferroptosis by targeting System Xc^-, a cystine-glutamate antiporter system. RSL3 is a ferroptosis inducer that inhibits glutathione peroxidase 4 (GPX4), a lipid peroxidase enzyme that employs glutathione for quenching lipid peroxides and directly inhibits ferroptosis (Figure S17A). Conversely, ferrostatin-1 (Fer-1) and liproxstatin-1 (Lip-1) are specific ferroptosis inhibitors that scavenge lipid peroxides and restore GSH levels (Figure S17A). We chose to combine these ferroptosis modulators with our lead molecules to witness the effect. Initial evaluation of canonical GPX4 inhibitor RSL3 robustly inhibited the growth of Huh-7 cells with an EC_{50} of 26 nM, and its combination with either Fer-1 or Lip-1 showed a tremendous prevention effect by more than 500-fold, thereby validating the ferroptosis assay system (Figures S17C and S17D). Whereas, combining our hits (IITK4001-IITK4004) with either Fer-1 or Lip-1 did not provide any significant protective effect (Figures S17D, S17F, and S18). Further, in our assessment, neither erastin nor RSL3 potentiated the cancer cell killing (in both Huh-7 and U2OS) by IITK4001-4004 (Figures S17B, S17C, S17F, and S18), thus dismissing the possibility of a ferroptosis cell killing mechanism for IITK4001-4004. In addition, ROS-mediated cancer cell death is known to trigger necroptosis and rapid cellular damage. However, cancer cell viability analysis for our hits in combination with necrostatin-1 (necroptosis inhibitor) showed little cell death prevention (Figure S18), thereby eliminating this possibility as well.

IITK4003/4004 induces mitochondrial dysfunction

Mitochondria, the powerhouse of cells is a sensitive organelle that responds to a sudden fluctuation of redox status. Upon exposure to toxic levels of ROS, mitochondrial membrane potential (MMP) is affected, which could be measured using established TMRM (Tetramethylrhodamine methyl ester)-mitochondria imaging by the reduction in TMRM fluorescence intensity (Figures 6A, 6B, and S19). We observed a considerable decrease in the labeling of mitochondria by TMRM in both Huh-7 and U2OS cells in the conditions treated with IITK4003/4004 and hydrogen peroxide alone or in combination (Figures 6A, 6B, and S19). Identical to the H_2DCF-DA assay, the cotreatment of IITK4003 or IITK4004 with peroxides and NAC inversely correlated with their mechanism as expected (Figures 6A and 6B). In parallel, we used MitoSOX green to capture the mitochondrial ROS accumulation (Figures 6A and 6C). We used a reported ROS generator and lipid peroxidation inducer, JCHD, as a positive control (Figures 6A and 6C).[46,47] Our molecules on their own diminished the MMP and drove low levels of mitochondrial ROS accumulation; however, upon exposure to H_2O_2, a sharp increase in the overall ROS level was detected (Figures 6A and 6C). Overall, these findings suggest that IITK4003/4004 drives ROS accumulation, which could impair mitochondrial function in cancer cells. Given that our lead molecules disrupt MMP and induce ROS accumulation in cells, we chose small molecule inhibitors of ETC complexes, rotenone (complex I),[52] antimycin A (complex III),[53] and sodium azide (NaN_3, complex IV)[54] to compare and assess the effect of IITK4003/4004 on mitochondrial function in cancer cells (Figures 6D, S20A, and S20B). One of the outcomes of mitochondrial functional inhibition is the depleted ATP levels. Our quantification of ATP levels in Huh-7 cells with lead molecules and canonical ETC inhibitors exhibited a profound decrease in ATP, assuring a parallel mitochondrial functional inhibition mechanism for IITK4003/4004 (Figures 6D and S20). Having established oxidative mitochondrial dysfunction in cells with our lead molecules, we set out to evaluate the effect of ROS modulators on the toxicity of IITK4003/4004 to Huh-7 cells. Therefore, we combined buthionine sulfoximine (BSO, a glutathione biosynthesis inhibitor, induces oxidative stress) and antioxidants (vitamin E [Vit-E] and NAC) with IITK4001-IITK4004 independently, to capture their effect on the proliferation of cancer cells (Figures 6E, 6F, and S21). We observed a uniform trend of dose-dependent enhancement of cell death with BSO and a protective effect by Vit-E/NAC for all the molecules tested (Figures 6E and 6F). This is effectively suggesting oxidative stress induction is a relevant molecular mechanism of our lead molecules.

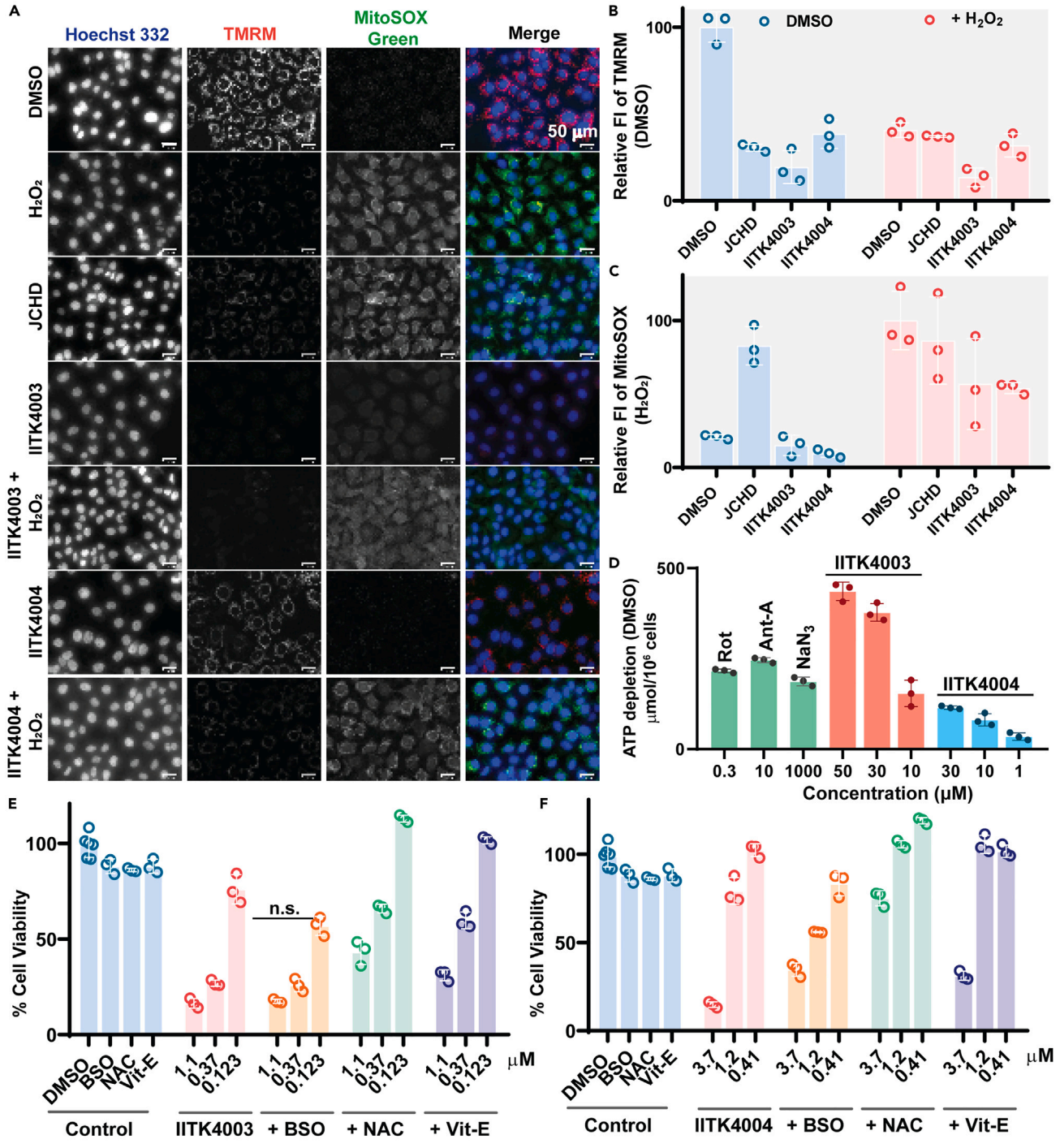

Figure 6. IITK4003/IITK4004-induced ROS accumulation led to mitochondrial dysfunction and correlated with ROS-mediated Huh-7 cell death

(A–C) Effect of indicated compounds and combinations on MMP in Huh-7 cells imaged using a potentiometric fluorophore, TMRM, and ROS accumulation with MitoSOX Green using fluorescence microscopy (A) and their relative fluorescence intensity quantified data (B, C). Scale bar: 25 µm.

(D) Reduction in the levels of ATP quantified using a luminescence-based Celltiter-Glo assay in Huh-7 cells upon treatment with indicated molecules.

(E and F) Effect of additional non-toxic dose of oxidants (BSO-50 µM) and antioxidant (Vit-E-300 µM, NAC-500 µM) on the cell viability of Huh-7 cells treated with IITK4003 (E) or IITK4004 (F) at indicated concentrations. Graphs B–F indicate mean ± SD. Data presented are representative of more than two independent replicates and a minimum of three technical replicates. Cell viability data are normalized relative to DMSO treatment control as 100%.

IITK4003/4004 trigger caspase cascade to induce apoptosis

Oxidative mitochondrial impairment leads to the release of mitochondrial proteins including cytochrome c into the cytosol, which are known to activate caspase cascade and trigger apoptosis.[55–57] Therefore, we used multiple sets of experiments including combination treatment cell viability studies, immunoblotting, and immunofluorescence imaging to capture the cell death mechanism (Figure 7). First, we investigated the effect of apoptosis, a programmed cell death inhibitor, QVD-OPh (a pan-caspase inhibitor), in combination with our lead molecules in Huh-7 and U2OS cells (Figures 7A and S23).[58,59] We observed profound rescue of cell death by QVD-OPh when combined with lead molecules, thereby hinting a likely apoptosis mechanism (Figure 7A).[60] Then, we conducted immunofluorescence imaging to visualize the apoptosis biomarkers in the cells treated with our molecules. We stained the cells for annexin-V (an apoptosis biomarker) and propidium iodide (PI, for tracking cell death) after treatment with our molecules (Figures 7B, 7C, S24, and S25). We found a remarkable increase in the staining for annexin-V and PI in cells treated with our molecules, and a cotreatment with QVD-OPh rescued the PI staining (Figures 7B, 7C, S24, and S25). Next, we performed immunoblotting for tracking the activation profiles of caspase-cascade-mediated apoptosis markers. First, we confirmed the release of mitochondrial cytochrome c (Cyt c) to the cytoplasm after treatment with our lead molecules and the positive control (Figure 7D). We observed a comparable effect on the release of cytochrome c for both the ligands as well as the complexes' treatment (IITK4001-IITK4004). Then, a time-dependent (4 h and 8 h) analysis of full-length caspase-3 and its activation to release cleaved caspase-3 indicated a sharp increase in the caspase-3 activation over time, and this was comparable to the positive control, staurosporine (Figures 7E, 7F, and S26). The subsequent effect of caspase-3 activation to trigger the cleavage of death substrate poly [ADP-ribose] polymerase 1 (PARP-1) exhibited a strong correlation with our lead-molecule-mediated apoptosis in two independent cell lines (Figures 7E, 7F, and S26). Interestingly, both the ligands (IITK4001 and IITK4002) were found to exert strong effect on the caspase-3 cleavage when compared to their respective complexes (Figures 7E and S26), which was comparable to that of positive control staurosporine in Huh-7 cells, and effect was found to be extending to PARP-1 cleavage. Whereas in U2OS cell line, we have observed a stronger band for cleaved caspase-3 and PARP-1 for the complex 4004 over the ligand IITK4002. Despite the relatively slight difference on the extent of caspase-cascade activation, both ligand and complexes were highly effective in preventing the cancer cell growth and induced apoptosis (Figures S7 and S22–S26). Collectively, the abovementioned set of experiments strongly suggests that our lead molecules induce mitochondrial dysfunction and released Cyt c into the cytoplasm to trigger the caspase cascade that promoted the intrinsic apoptotic cell death mechanism in cancer cells.

Pan-cancer activity and 3D-spheroid growth inhibition by IITK4003/4004

Further, to emphasize the generality of IITK4003/IITK4004 to act as proliferation inhibitor of various cancer phenotypes, we have screened the indicated molecules against a panel of 10 more cancer phenotypes in addition to Huh-7 and U2OS (Table 1, Figure S27). We observed growth inhibition of cancer cells within a range of 0.3–3.5 μM EC_{50} against all the cancer lines investigated. We found Huh-7 cells to be highly sensitive to IITK4003 with an EC_{50} at 340 nM concentration, whereas other cancer phenotypes exhibited comparable sensitivity. Among the hepatocellular carcinoma (HCC) cells, the sensitivity of Huh-7 cells was nearly 10-fold higher than HepG2 cells (Table 1, Figure S27). These drastic differences in selectivity could be attributed to several factors including genetic and metabolic differences and higher lipogenesis in Huh-7 cells over other hepatoma cells,[61–63] which is an interesting lead for future explorations. In the case of IITK4004, the molecules exhibited comparable cell-killing potency (2.2–3.5 μM) with all the cancer cell lines tested (Table 1, Figure S27). Extending the studies to 3D-cell models such as spheroids will help us capture the ability of our molecules to penetrate the tissue-like structure and inhibit their growth. Therefore, we have generated 3D-spheroids of HepG2 cells and treated them with mitomycin as a positive control to establish a functional assay system. Then the treatment of spheroids with IITK4003 and IITK4004 showed an excellent reduction in the scaffold size of spheroids in a dose-dependent fashion (Figures 8A–8C). These results together highlight that these molecules can prevent multiple cancer phenotypes and they can be successful in inhibiting tumor growth *in vivo* as indicated by volume reduction in the prototype, 3D-spheroids.

Nanocarrier potentiating the activity of IITK4003/4004 in liver cancer cells

Our studies for IITK4003 in multiple cancer phenotypes showed a variable EC_{50} (0.34–3.3 μM, a 10-fold difference), whereas a comparable EC_{50} was recorded for IITK4004 (2.2–3.9 μM) in all the cell lines investigated (Table 1, Figure S26). At higher concentrations, we found aqueous solubility issues for IITK4003 over IITK4004; therefore, it was suspected that the differential EC_{50} in various cell lines could be an outcome of differential cell permeability. Hence, to evaluate this possibility, we have performed inductively coupled plasma resonance mass spectrometry (ICP-MS) and energy dispersive X-ray spectroscopy and scanning electron microscopy (EDX-SEM) of HUH-7 cell treated with DMOS or lead metal complexes (20 μM, Figures S28 and S29). We have observed a distinct increase in the iron levels in both ICP-MS and EDX-SEM analysis in the metal-complex-treated conditions. Indeed, under comparable conditions, the iron level was quantified to be slightly higher in the case of IITK4004 over IITK4003, thereby reflecting on the differential aqueous solubility impacting cell permeability of the complexes. Therefore, to improve the local concentration of the metal complexes intracellularly, a polymeric nanosized drug carrier was synthesized for the effective delivery of IITK4003 and IITK4004, which would overcome the problem associated with water solubility and cell permeability. A water-in-oil-in-water emulsion method (Scheme S3) was employed for the preparation of the nanocarriers (NCs) using an amphiphilic, diblock amphiphilic copolymer carboxylic acid poly (ethylene glycol)-block-poly(lactide-co-glycolide) (PLGA-b-PEG-COOH). The molecules of interest, IITK4003 and IITK4004, were added to the polymer solution at the first step of preparation of NCs, which led to an effective entrapment of molecules, presumably inside the hydrophobic core of the nanocarriers (Scheme S4). Dynamic-light-scattering-based investigation revealed that the effective hydrodynamic diameter of synthesized NCs was 186 ± 2.5 nm. It was noticed that there was no significant change in effective

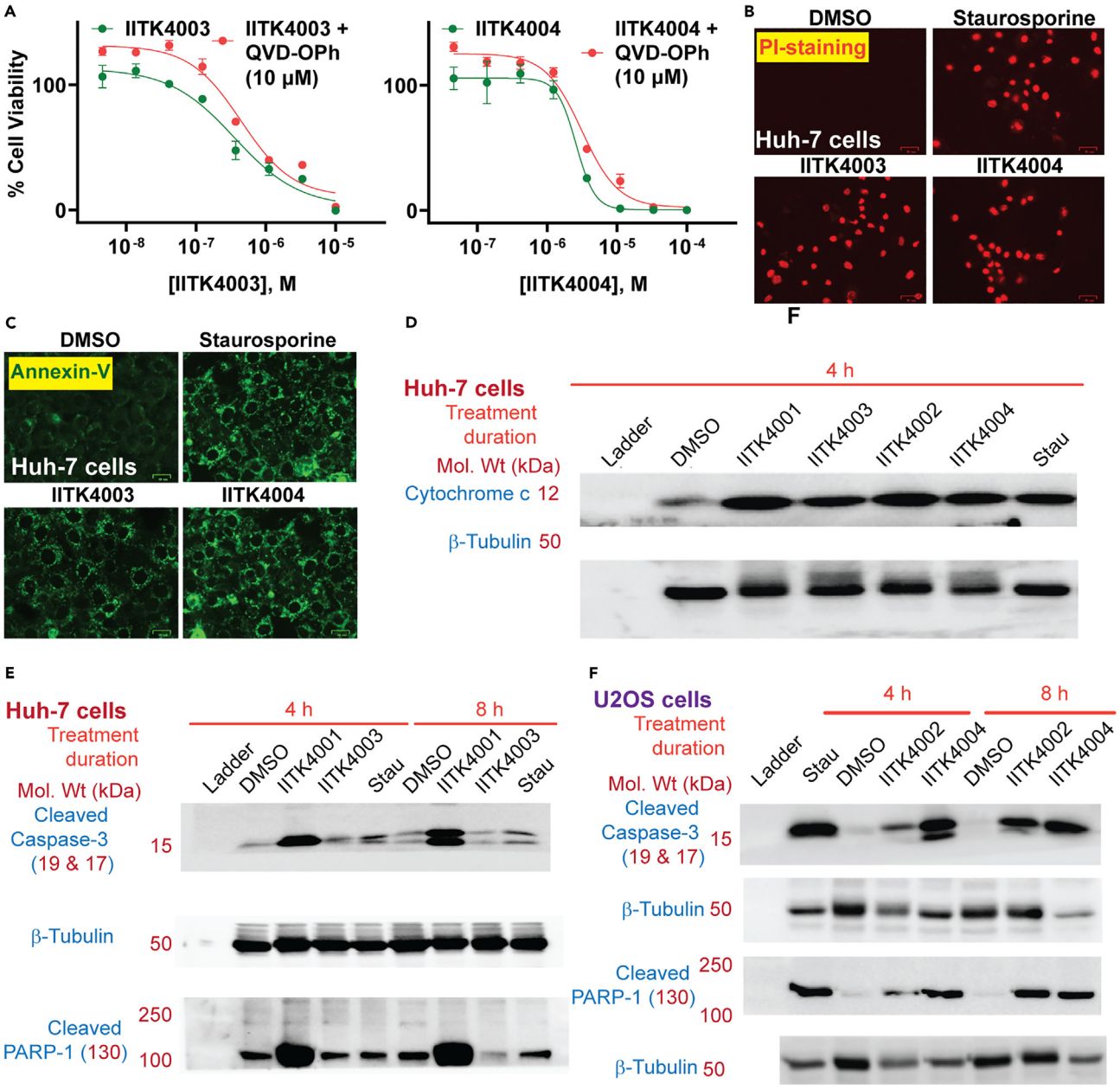

Figure 7. IITK4003/IITK4004 triggers the caspase cascade to promote apoptosis in cancer cells

(A) Cell viability studies of Huh-cells upon cotreatment of apoptosis inhibitor QVD-OPh (10 μM, A) with our lead molecules.

(B and C) Induction of apoptosis in Huh-7 (E) and U2OS (F) cells by IITK4001/4003 (20 μM) and staurosporine (250 nM) was captured using a fluorescence imaging of propidium iodide (PI)-stained nuclei and immunostaining for an apoptosis marker, Annexin-V.

(D–F) Immunoblotting for indicated apoptosis markers in Huh-7 (D, E) and U2OS cells (F) after 4 h and 8 h of treatment with IITK4001-IITK4004 (30 μm) and the positive control staurosporine (100 nm). Protein concentration in each lane was 20 μg; all molecules were used at 30 μM, except Stau: staurosporine, 100 nM). Graphs A–D indicate mean ± SD. Data presented are performed in two independent cell lines and are representative of more than two independent experiments with a minimum of three technical replicates. Cell viability data are normalized relative to DMSO treatment control as 100%.

hydrodynamic diameter of NCs on loading of the IITK4003 and IITK4004 in nanocarriers, called as NC/IITK4003 and NC/IITK4004, respectively (Figures 9A and S30). The effective hydrodynamic diameter of NC/IITK4003 and NC/IITK4004 was 184 ± 1.5 nm and 183 ± 7.5 nm, respectively. The polydispersity index (PDI) values of NCs, NC/IITK4003 and NC/IITK4004 nanosuspension, were found to be 0.18 ± 0.01, 0.14 ± 0.01 and 0.23 ± 0.02, respectively (Figure 9B). These low PDI values implied the homogeneous nature of the polymeric nanocarriers, which was retained even after loading IITK4003 and IITK4004. This observation was also supported by the intensity vs. size distribution plot as

Table 1. Cell viability analysis of various cancer cell lines with IITK4003 and IITK4004 (EC_{50} values with an average SD of ±0.1 μM for IITK4003 in Huh-7)

Cancer cell line	IITK4003 (μM)	IITK4004 (μM)
Huh-7	0.34	2.2
Huh-7[a]	0.11	1.9
HepG2	4.87	3.07
HepG2[a]	0.42	2.8
HEK293	3.82	7.6
A549	1.99	2.3
Jurkat-6	1.6	2.2
MCF7	1.41	2.7
MDA-MB-231	2.1	2.4
U2OS	2.10	2.3
A375	ND	2.9
HCT116	ND	2.6
PC3	ND	3.5
RPMI 8226	ND	2.3
U87MG	ND	4.0

[a]EC_{50} of the IITK4003/IITK4004 encapsulated in nanocarrier; N.d., not determined. Cancer cell lines: A549: lung carcinoma epithelial cells; HepG2 & Huh-7: hepatocellular carcinoma; Jurkat J6: acute T-cell leukemia; MCF7: breast cancer MDA-MB-231; triple negative breast cancer; U2OS, osteosarcoma; A375, melanoma; HCT-116, colon cancer; PC3, prostate cancer; RPMI 8226, B lymphocytes; U87MG, glioblastoma.

represented in Figure 8C for NCs and NC/IITK4003, NC/IITK4004, and their imaging (Figure 9D). Further, the loaded amount of IITK4003 and IITK4004 was quantified by analyzing the absorbance vs. concentration standard plot. It was found that the loaded concentration of IITK4003 and IITK4004 in NCs was 34.8 and 194 μM, respectively (Figures 9E and 9F). This quantification deciphered that the entrapment of two water insoluble molecules, IITK4003 and IITK4004, inside polymeric NCs brought these molecules into aqueous suspension in significantly higher concentration and eventually be available to the biological system for uptake possibly through endocytosis.[64–66] These lead-molecule-encapsulated nanocarriers were evaluated in both Huh-7 and HepG2 cells for their antiproliferative activity. NC/IITK4003 exhibited nearly a 4-fold (0.43–0.11 μM) in Huh-7 and 12-fold (4.87–0.42 μM) enhancement in EC_{50} HepG2 cells (Figures 9G–9K). Under comparable conditions, we found no significant difference in the EC_{50} for IITK4004 between the pristine treatment or nano-encapsulated form NC/IITK4004. Collectively, our effort to enhance the effective delivery of IITK4003 through nanoencapsulation resulted in the identification of exceptionally potent growth inhibition of Huh-7 cells at 110 nM EC_{50}.

DISCUSSION

Drug resistance in cancer is a serious global threat, and identification of novel therapeutic interventions is a high priority. Emerging technologies including PROTACs (small-molecules-based proteolysis activating chimeras for target protein degradation), CRISPR-Cas systems (for genetic manipulations), and antibody-drug conjugates offer promises. In parallel, classical drug discovery approaches using small molecules to target specific disease-relevant proteins and/or cellular functional machinery have also continued to evolve. Cisplatin set the foundation for metal-based therapeutics, and it was approved nearly five decades ago by US-FDA (1978) for cancer treatment. Since then, only fewer metal complexes entered clinical trials, and overall metal-complex-based cancer therapeutics development remains underdeveloped. Recently, modulation of intracellular metal ion levels to alter redox homeostasis is emerging as a potential therapeutic modality to prevent cancer progression.[25,26] Targeting this redox sensitivity, several ruthenium-based compounds with systematically varied ligands core have been developed as potential anticancer therapies.[10–12,67–75] Moreover, iron complexes of ferrocene, salen, and *N*-heterocyclic ligands are developed as potential anticancer agents, exerting their effects by triggering reactive oxygen species (ROS) production within cancerous cells at micromolar concentrations.[13–16] We identified IITK4001 and IITK4002 as a potential candidate for promoting apoptosis in cancer cells at 110 nM potency. We provided a comprehensive understanding of IITK4001/4002 as trapping intracellular iron by complexation and ROS-mediated mitochondrial function impairment to promote apoptosis in cells (Figure 10). Interestingly, there is no literature evidence of the characterization of reactive iron oxo species generated by IITK4004 in water, possibly owing to the challenge associated with their poor stability in aqueous milieu. However, high-valent reactive metal oxo species in organic solvents and their utility in catalysis such as oxygen atom transfer reactions are known.[39] One of the key aspects is we have successfully characterized the short-lived high-valent Fe(IV)=O intermediates in water to set the literature precedence. Notably, IITK4003/4004-mediated ROS generation and accumulation of lipid peroxide did not trigger ferroptosis. Perhaps, the concentration of lipid peroxide accumulation induced by our molecules is not sufficient to trigger ferroptosis, which is also reflected in the absence of necroptotic cell death (typically activated with excess ROS).[76,77] Mitochondrial components such as cytochrome c released into cytoplasm leading to the activation of caspase cascade to trigger apoptosis augurs well with our mechanism since our

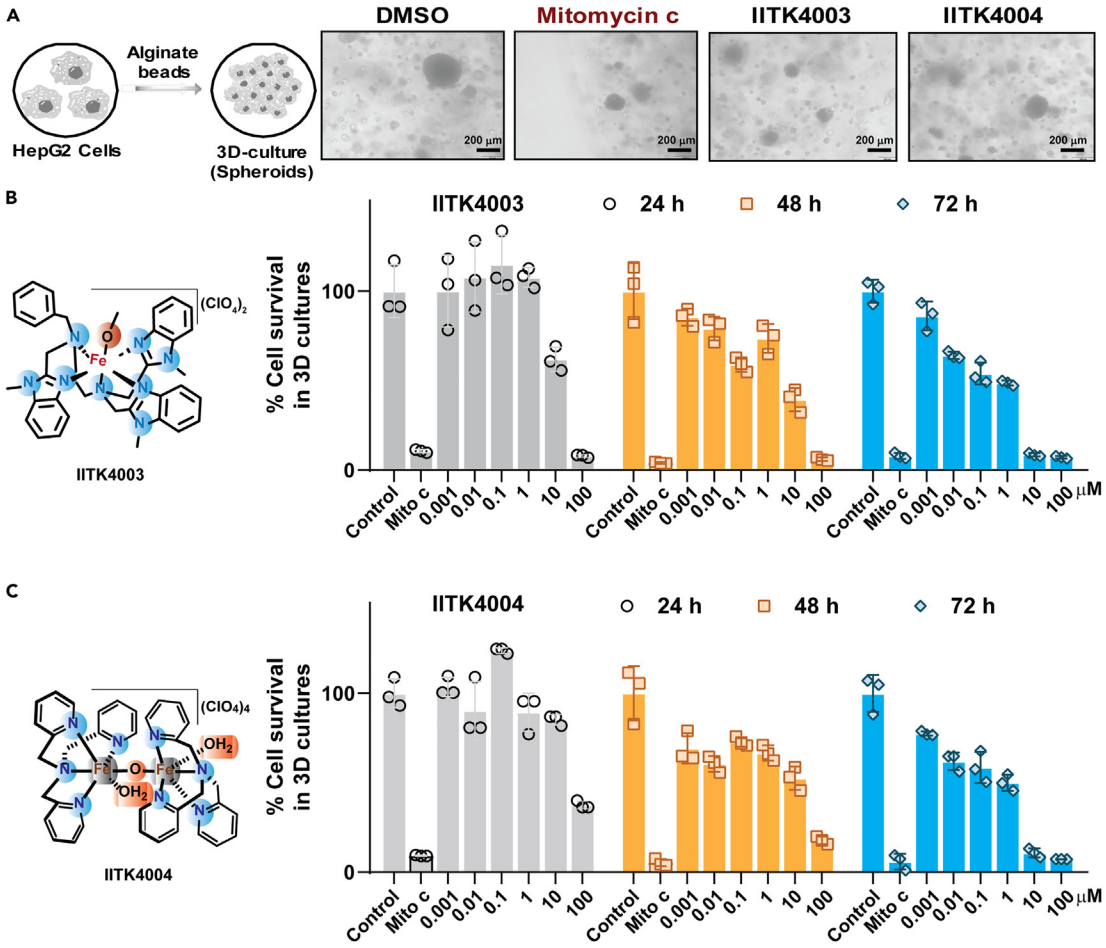

Figure 8. Our lead molecules IITK4003/IITK4004 reduced the 3D-spheroid volume and dose-dependently inhibited their growth

(A) Schematic and images of HepG2 cells spheroids generated out of 3D-culture and their treatment with indicated molecules after 72 h. Scale bar: 200 µm. (B and C) 3D-culture cell viability was assessed during their treatment with IITK4003/IITK4004 for 24, 48, and 72 h using MTT assay. Graphs B and C indicate mean ± SD. Data presented in (A–C) are representative of two or more independent experiments with a minimum of three technical replicates. Cell viability data are normalized relative to DMSO treatment control as 100%.

lead molecules were found to promote mitochondrial dysfunction. Though we obtained an excellent EC_{50} for IITK4003 in Huh-7 cells and were good at reducing the size of HepG2-spheroids, we observed solubility issues at higher concentrations. Initially, we suspected the solubility and cell permeability could potentially dictate the EC_{50} of IITK4003 in various cell lines. A head-to-head comparison of IITK4003 and its nano-encapsulated version NC/IITK4003 in both Huh-7 and HepG2 exhibited a remarkable improvement in the overall potency indeed confirming the effective delivery of IITK4003 could be a serious contributor to improve the efficiency of the molecules. In summary, our study suggests that an angle of metal trapping and subsequent chemical reactivity and improvisation of local drug concentration could be used for heterocyclic molecules' biological activity and to study their mechanism of action.

Limitation of the study

We report that nitrogen-based heterocyclic scaffolds form complexes with iron to induce antiproliferative activity in cancer cells. The proposal was established by synthesizing authentic iron complexes and evaluating them for their antiproliferative activity and their mechanism of action studies. However, proving the complexation with intracellular iron was not possible due to minute change in the intracellular iron concentration with IITK4002 addition (our ligands are active in low micromolar concentrations and cellular iron levels ~20 µM). This could be addressed by synthesizing structurally close turn-on fluorescent probes for intracellular iron, which is a scope for future research. Further, though the biological activity of IITK4001 was mimicked in the respective iron complex, IITK4003's outstanding response in cells could not be studied as the solubility issues associated with IITK4001 under physiological conditions have hampered our plans of establishing iron complexation mechanism inside cell. Additional modifications in the structure to enhance the solubility of IITK4001 to improve the potency and to decipher the mechanism of action is another direction to pursue. Future experiments could include ICP-MS analysis of HEK293 cells treated with lead

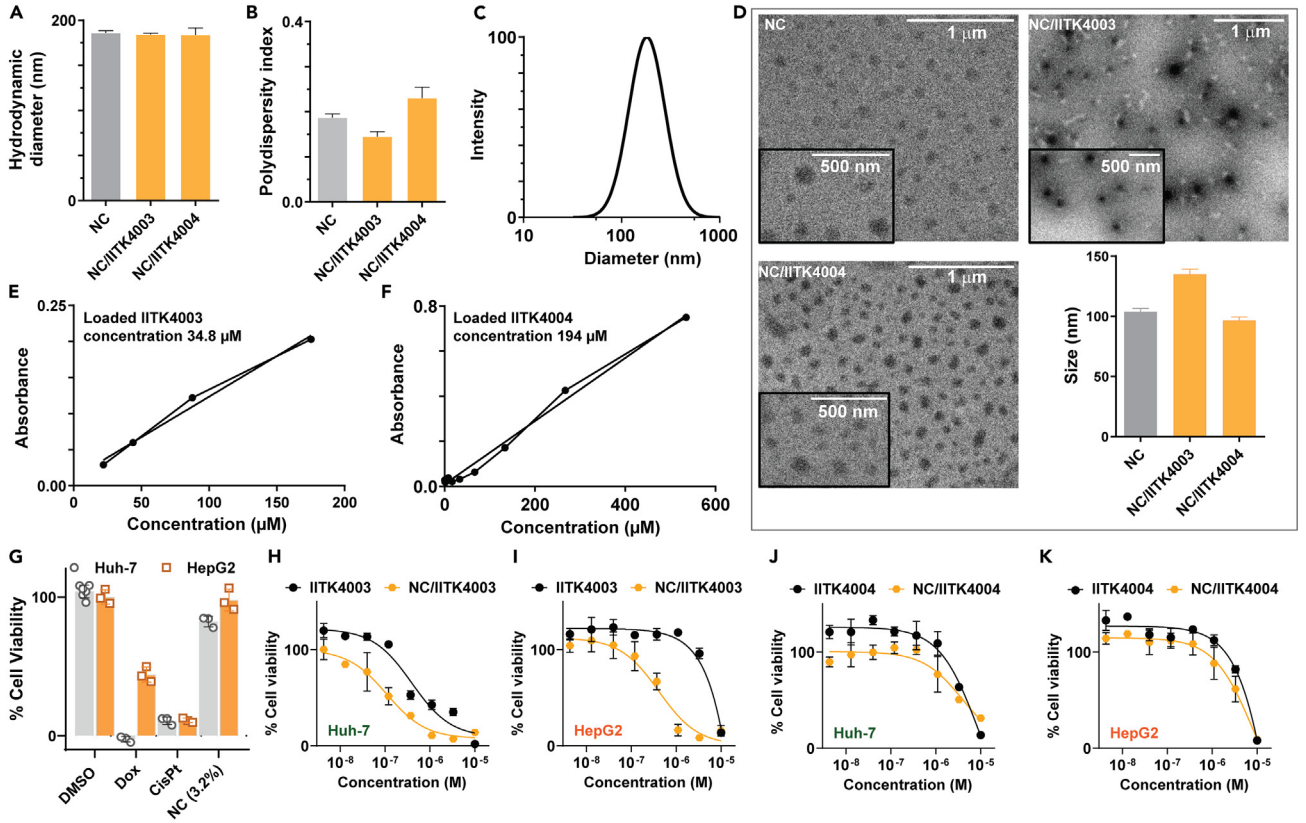

Figure 9. Nanocarrier-mediated drug delivery potentiated the antiproliferative activity of IITK4003 in liver cancer cell lines

(A) The hydrodynamic diameter of NCs, NC/IITK4003, and NC/IITK4004.

(B) Polydispersity index of NCs, NC/IITK4003, and NC/IITK4004.

(C) Representative intensity vs. diameter size distribution plot for NCs.

(D) Representative TEM image of NCs, NC/IITK4003 and NC/IITK4004. Anhydrous size of NCs, NC/IITK4003 and NC/IITK4004 samples, as obtained from respective multiple TEM images.

(E and F) Representative absorbance vs. concentration standard plot for quantification of (E) IITK4003 loading and (F) IITK4004 loading.

(G–K) Cell viability studies of Huh-7 and U2OS cells upon treatment with IITK4003/4004, their nano-encapsulated forms and controls (G), IITK4003 and NC/IITK4003 (H, I), IITK4004 and NC/IITK4004 (J, K) in Huh-7 (data colored in gray) and U2OS (data colored in orange) cells. Graphs A, B, D, and G–K indicate mean ± SD. Data presented in G–K are representative of two or more independent experiments with a minimum of three technical replicates in each cell line. Cell viability data are normalized relative to DMSO treatment control as 100%.

compounds and nanocarriers loaded with iron complexes to gather more insights on the accumulation of iron on selective toxicity to cancer cells over the normal cells.

STAR★METHODS

Detailed methods are provided in the online version of this paper and include the following:

- KEY RESOURCES TABLE
- RESOURCE AVAILABILITY
  - Lead contact
  - Materials availability
  - Data and code availability
- EXPERIMENTAL MODEL AND STUDY PARTICIPANT DETAILS
  - Cell lines
- METHOD DETAILS
  - General information
  - Synthesis and characterization
  - HPLC for purity analysis

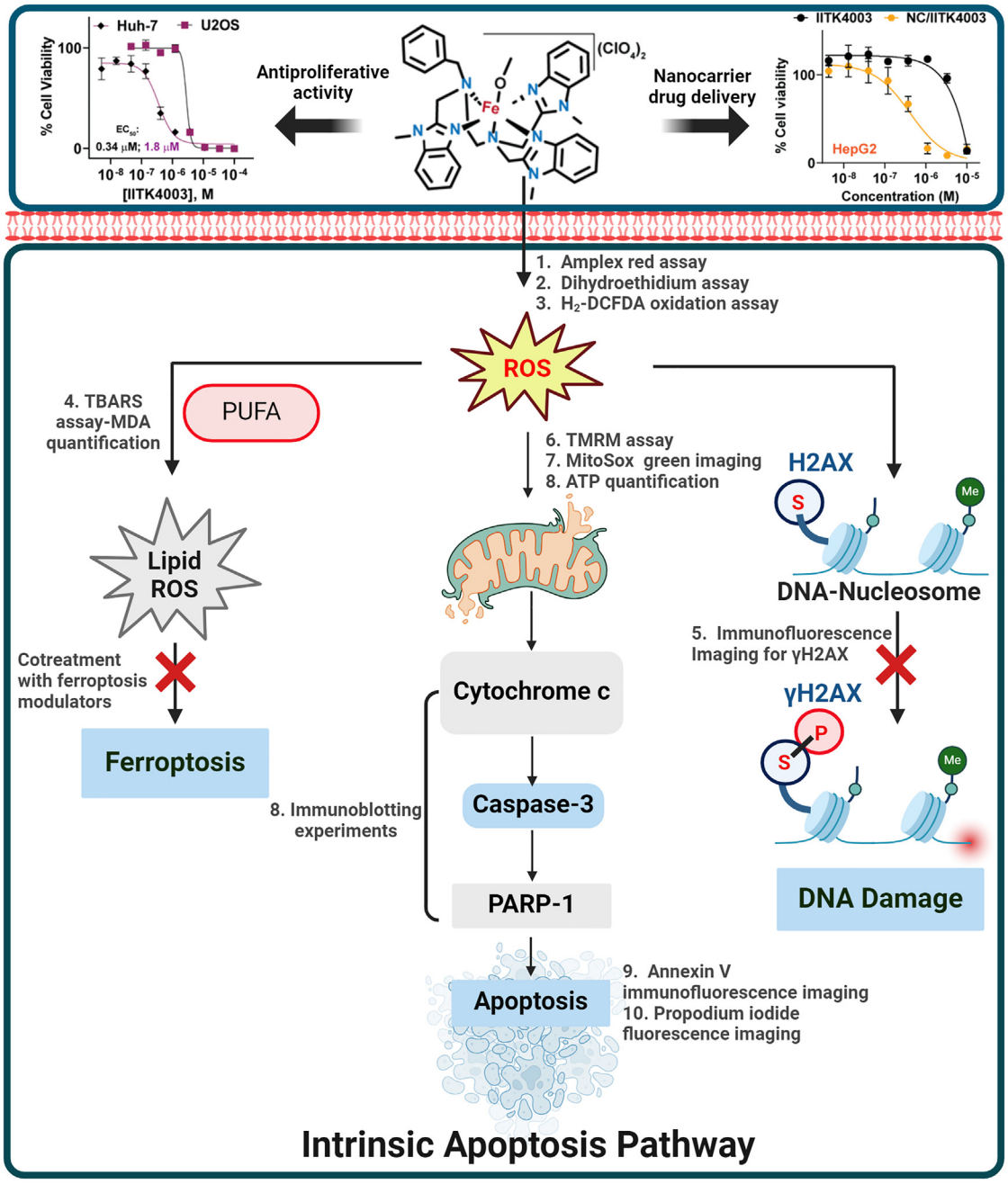

Figure 10. Summary figure capturing the molecular mechanism of iron complexes (IITK4003) in activating intrinsic apoptosis pathway

The set of experiments conducted to establish the respective molecular mechanism of our lead molecule are summarized on the arrow. ROS generated by our metal complexes in cancer cells (Amplex Red assay, DHE assay, and H2-DCFDA assay) did not induce DNA damage and was captured by monitoring the phosphorylation H2AX (immunofluorescence imaging). While the lipid peroxide accumulation was detected (TBARS assay-MDA quantification) in cancer cells upon treatment with our complexes, combination cell viability experiments with ferroptosis modulators indicated no ferroptosis mechanism. ROS-induced mitochondrial dysfunction (TMRM assay, MitoSox green imaging, ATP quantification) led to the activation of intrinsic apoptosis cascade—cytochrome c release—activations of caspase-3—PARP-1 cleavage—resulting in apoptotic cell death.

- Cell viability assessment: General protocol
- Concentrations of compounds used in the cell viability assays
- Mitochondrial ROS and membrane potential assessment
- ROS quantification by using DCFDA

- Cellular ATP quantification
- Amplex red assay
- Dihydroethidine (DHE) oxidation assay
- Propidium iodide staining and annexin-V immunostaining
- Western blotting
- TBARS assay
- Pγ-H2AX immunostaining
- 3D culture using sodium alginate bead
- In vitro cell viability assay of 3D cultures
- EDX-SEM analysis
- ICP-MS analysis
- Synthesis of polymeric nanocarriers
- Characterization of polymeric nanocarriers
- Quantification of drug loading
- Abbreviations

● QUANTIFICATION AND STATISTICAL ANALYSIS

SUPPLEMENTAL INFORMATION

Supplemental information can be found online at https://doi.org/10.1016/j.isci.2024.109899.

ACKNOWLEDGMENTS

We thank Prof J. G. Rao and Prof B. Ateeq for gifting us the caspase and PAPR-1 antibody, and Dr. Nitin Mohan for gifting cell lines from Department of biological Science and engineering, IIT Kanpur. Dr. Amit Lahiri, CSIR-CDRI Lucknow, is thanked for the donation of Cytochrome c antibody. Department of Chemistry, IIT Kanpur for the research facility.

Funding: Doctoral fellowship from IITK for S.K.V. and R.K., CSIR for S.G., DST-Inspire for S.S. are acknowledged. S.K. and D.A. acknowledge a fellowship from DBT-IYBA and for financial support. This work was supported by Department of Biotechnology, DBT-IYBA grant (BT/12/IYBA/2019/07), Extramural Research grant from Council of Scientific and Industrial Research (CSIR), India (02(366)/19/EMR-II), CRG from DST-Science and Engineering Research Board (SERB, CRG/2021/004787), Indian Council of Medical Research (ICMR, AMR/ADHOC/296/2022-ECD-II), SERB (CRG/2019/003058), and CSIR (01(3050)/21/EMR-II).

AUTHOR CONTRIBUTIONS

S.K.V., S.K., and S.S. performed the cell viability screening. S.G., R.K., D.A., and A.D. synthesized and characterized metal complexes and analyzed their reactivity profiles. S.K.V. conducted combination experiments, lipid peroxide measurement, microscopy, and western blotting studies. N.C., S.K.V., D.A., and S.K.M. conducted all the experiments related to nanocarrier synthesis, characterizations, and biological studies. P.Y.T. and M.B.J. performed 3D-spheroids studies. D.A. wrote the manuscript, and all the authors provided intellectual input, edited, and approved the final manuscript.

DECLARATION OF INTERESTS

The authors declare no competing interests.

Received: January 22, 2024
Revised: March 21, 2024
Accepted: May 1, 2024
Published: May 3, 2024

REFERENCES

1. Rosenberg, B., VanCamp, L., Trosko, J.E., and Mansour, V.H. (1969). Platinum compounds: a new class of potent antitumour agents. Nature *222*, 385–386. https://doi.org/10.1038/222385a0.
2. Jamieson, E.R., and Lippard, S.J. (1999). Structure, Recognition, and Processing of Cisplatin–DNA Adducts. Chem. Rev. *99*, 2467–2498. https://doi.org/10.1021/cr980421n.
3. Eskandari, A., Kundu, A., Ghosh, S., and Suntharalingam, K. (2019). A Triangular Platinum(II) Multinuclear Complex with Cytotoxicity Towards Breast Cancer Stem Cells. Angew. Chem. Int. Ed. *58*, 12059–12064. https://doi.org/10.1002/anie.201905389.
4. Jin, S., Muhammad, N., Sun, Y., Tan, Y., Yuan, H., Song, D., Guo, Z., and Wang, X. (2020). Multispecific Platinum(IV) Complex Deters Breast Cancer via Interposing Inflammation and Immunosuppression as an Inhibitor of COX-2 and PD-L1. Angew. Chem. Int. Ed. *59*, 23313–23321. https://doi.org/10.1002/anie.202011273.
5. Laws, K., Bineva-Todd, G., Eskandari, A., Lu, C., O'Reilly, N., and Suntharalingam, K. (2018). A Copper(II) Phenanthroline Metallopeptide That Targets and Disrupts Mitochondrial Function in Breast Cancer Stem Cells. Angew. Chem. Int. Ed. *57*, 287–291. https://doi.org/10.1002/anie.201710910.
6. Xiao, Z., Johnson, A., Singh, K., and Suntharalingam, K. (2021). The Discrete Breast Cancer Stem Cell Mammosphere Activity of Group 10-Bis(azadiphosphine)

Metal Complexes. Angew. Chem. Int. Ed. *60*, 6704–6709. https://doi.org/10.1002/anie.202014242.
7. Clarke, M.J., Zhu, F., and Frasca, D.R. (1999). Non-Platinum Chemotherapeutic Metallopharmaceuticals. Chem. Rev. *99*, 2511–2534. https://doi.org/10.1021/cr9804238.
8. Eskandari, A., and Suntharalingam, K. (2019). A reactive oxygen species-generating, cancer stem cell-potent manganese(ii) complex and its encapsulation into polymeric nanoparticles. Chem. Sci. *10*, 7792–7800. https://doi.org/10.1039/C9SC01275C.
9. Suntharalingam, K., Lin, W., Johnstone, T.C., Bruno, P.M., Zheng, Y.-R., Hemann, M.T., and Lippard, S.J. (2014). A Breast Cancer Stem Cell-Selective, Mammospheres-Potent Osmium(VI) Nitrido Complex. J. Am. Chem. Soc. *136*, 14413–14416. https://doi.org/10.1021/ja508808v.
10. Gill, M.R., Cecchin, D., Walker, M.G., Mulla, R.S., Battaglia, G., Smythe, C., and Thomas, J.A. (2013). Targeting the endoplasmic reticulum with a membrane-interactive luminescent ruthenium(ii) polypyridyl complex†Electronic supplementary information (ESI) available: Experimental details, characterization of 2 and Fig. S1-S6. See DOI: 10.1039/c3sc51725jClick here for additional data file. Chem. Sci. *4*, 4512–4519. https://doi.org/10.1039/c3sc51725j.
11. Clavel, C.M., Păunescu, E., Nowak-Sliwinska, P., Griffioen, A.W., Scopelliti, R., and Dyson, P.J. (2015). Modulating the Anticancer Activity of Ruthenium(II)-Arene Complexes. J. Med. Chem. *58*, 3356–3365. https://doi.org/10.1021/jm501655t.
12. Pettinari, R., Pettinari, C., Marchetti, F., Skelton, B.W., White, A.H., Bonfili, L., Cuccioloni, M., Mozzicafreddo, M., Cecarini, V., Angeletti, M., et al. (2014). Arene-ruthenium(II) acylpyrazolonato complexes: apoptosis-promoting effects on human cancer cells. J. Med. Chem. *57*, 4532–4542. https://doi.org/10.1021/jm500458c.
13. Szlasa, W., Gachowska, M., Kiszka, K., Rakoczy, K., Kiełbik, A., Wala, K., Puchała, J., Chorążykiewicz, K., Saczko, J., and Kulbacka, J. (2022). Iron chelates in the anticancer therapy. Chem. Pap. *76*, 1285–1294. https://doi.org/10.1007/s11696-021-02001-2.
14. Bouché, M., Hognon, C., Grandemange, S., Monari, A., and Gros, P.C. (2020). Recent advances in iron-complexes as drug candidates for cancer therapy: reactivity, mechanism of action and metabolites. Dalton Trans. *49*, 11451–11466. https://doi.org/10.1039/D0DT02135K.
15. Basu, U., Roy, M., and Chakravarty, A.R. (2020). Recent advances in the chemistry of iron-based chemotherapeutic agents. Coord. Chem. Rev. *417*, 213339. https://doi.org/10.1016/j.ccr.2020.213339.
16. Wani, W.A., Baig, U., Shreaz, S., Shiekh, R.A., Iqbal, P.F., Jameel, E., Ahmad, A., Mohd-Setapar, S.H., Mushtaque, M., and Ting Hun, L. (2016). Recent advances in iron complexes as potential anticancer agents. New J. Chem. *40*, 1063–1090. https://doi.org/10.1039/C5NJ01449B.
17. Hentze, M.W., Muckenthaler, M.U., Galy, B., and Camaschella, C. (2010). Two to Tango: Regulation of Mammalian Iron Metabolism. Cell *142*, 24–38. https://doi.org/10.1016/j.cell.2010.06.028.
18. Bogdan, A.R., Miyazawa, M., Hashimoto, K., and Tsuji, Y. (2016). Regulators of Iron Homeostasis: New Players in Metabolism, Cell Death, and Disease. Trends Biochem. Sci. *41*, 274–286. https://doi.org/10.1016/j.tibs.2015.11.012.
19. Zhang, Y., He, J., Jin, J., and Ren, C. (2022). Recent advances in the application of metallomics in diagnosis and prognosis of human cancer. Metallomics *14*, mfac037. https://doi.org/10.1093/mtomcs/mfac037.
20. Abedi, M., and Rahgozar, S. (2022). Puzzling out iron complications in cancer drug resistance. Crit. Rev. Oncol. Hematol. *178*, 103772. https://doi.org/10.1016/j.critrevonc.2022.103772.
21. Andrews, N.C. (2000). Iron homeostasis: insights from genetics and animal models. Nat. Rev. Genet. *1*, 208–217. https://doi.org/10.1038/35042073.
22. Shen, Y., Zhang, B., Su, Y., Badshah, S.A., Wang, X., Li, X., Xue, Y., Xie, L., Wang, Z., Yang, Z., et al. (2020). Iron Promotes Dihydroartemisinin Cytotoxicity via ROS Production and Blockade of Autophagic Flux via Lysosomal Damage in Osteosarcoma. Front. Pharmacol. *11*, 444. https://doi.org/10.3389/fphar.2020.00444.
23. Raza, M., Chakraborty, S., Choudhury, M., Ghosh, P.C., and Nag, A. (2014). Cellular Iron Homeostasis and Therapeutic Implications of Iron Chelators in Cancer. Curr. Pharm. Biotechnol. *15*, 1125–1140.
24. Kew, M.C. (2009). Hepatic iron overload and hepatocellular carcinoma. Cancer Lett. *286*, 38–43. https://doi.org/10.1016/j.canlet.2008.11.001.
25. Tsvetkov, P., Coy, S., Petrova, B., Dreishpoon, M., Verma, A., Abdusamad, M., Rossen, J., Joesch-Cohen, L., Humeidi, R., Spangler, R.D., et al. (2022). Copper induces cell death by targeting lipoylated TCA cycle proteins. Science (New York, N.Y.) *375*, 1254–1261. https://doi.org/10.1126/science.abf0529.
26. Cui, L., Gouw, A.M., LaGory, E.L., Guo, S., Attarwala, N., Tang, Y., Qi, J., Chen, Y.-S., Gao, Z., Casey, K.M., et al. (2021). Mitochondrial copper depletion suppresses triple-negative breast cancer in mice. Nat. Biotechnol. *39*, 357–367. https://doi.org/10.1038/s41587-020-0707-9.
27. Ramchandani, D., Berisa, M., Tavarez, D.A., Li, Z., Miele, M., Bai, Y., Lee, S.B., Ban, Y., Dephoure, N., Hendrickson, R.C., et al. (2021). Copper depletion modulates mitochondrial oxidative phosphorylation to impair triple negative breast cancer metastasis. Nat. Commun. *12*, 7311. https://doi.org/10.1038/s41467-021-27559-z.
28. Warburg, O., Wind, F., and Negelein, E. (1927). The metabolism of tumours in the body. J. Gen. Physiol. *8*, 519–530. https://doi.org/10.1085/jgp.8.6.519.
29. Bravin, C., Badetti, E., Licini, G., and Zonta, C. (2021). Tris(2-pyridylmethyl)amines as emerging scaffold in supramolecular chemistry. Coord. Chem. Rev. *427*, 213558. https://doi.org/10.1016/j.ccr.2020.213558.
30. Hentze, M.W., Muckenthaler, M.U., and Andrews, N.C. (2004). Balancing acts: molecular control of mammalian iron metabolism. Cell *117*, 285–297. https://doi.org/10.1016/s0092-8674(04)00343-5.
31. Liu, J., Chakraborty, S., Hosseinzadeh, P., Yu, Y., Tian, S., Petrik, I., Bhagi, A., and Lu, Y. (2014). Metalloproteins Containing Cytochrome, Iron–Sulfur, or Copper Redox Centers. Chem. Rev. *114*, 4366–4469. https://doi.org/10.1021/cr400479b.
32. Papanikolaou, G., and Pantopoulos, K. (2005). Iron metabolism and toxicity. Toxicol. Appl. Pharmacol. *202*, 199–211. https://doi.org/10.1016/j.taap.2004.06.021.
33. Nagao, H., Komeda, N., Mukaida, M., Suzuki, M., and Tanaka, K. (1996). Structural and Electrochemical Comparison of Copper(II) Complexes with Tripodal Ligands. Inorg. Chem. *35*, 6809–6815. https://doi.org/10.1021/ic960303n.
34. Nanthakumar, A., Fox, S., Murthy, N.N., and Karlin, K.D. (1997). Inferences from the 1H-NMR Spectroscopic Study of an Antiferromagnetically Coupled Heterobinuclear Fe(III)−(X)−Cu(II) S = 2 Spin System (X = O2-OH-). J. Am. Chem. Soc. *119*, 3898–3906. https://doi.org/10.1021/ja962404q.
35. Szajna, E., Dobrowolski, P., Fuller, A.L., Arif, A.M., and Berreau, L.M. (2004). NMR Studies of Mononuclear Octahedral Ni(II) Complexes Supported by Tris((2-pyridyl)methyl)amine-Type Ligands. Inorg. Chem. *43*, 3988–3997. https://doi.org/10.1021/ic040002a.
36. Dharmaraja, A.T. (2017). Role of Reactive Oxygen Species (ROS) in Therapeutics and Drug Resistance in Cancer and Bacteria. J. Med. Chem. *60*, 3221–3240. https://doi.org/10.1021/acs.jmedchem.6b01243.
37. Dickinson, B.C., and Chang, C.J. (2011). Chemistry and biology of reactive oxygen species in signaling or stress responses. Nat. Chem. Biol. *7*, 504–511. https://doi.org/10.1038/nchembio.607.
38. D'Autréaux, B., and Toledano, M.B. (2007). ROS as signalling molecules: mechanisms that generate specificity in ROS homeostasis. Nat. Rev. Mol. Cell Biol. *8*, 813–824. https://doi.org/10.1038/nrm2256.
39. Kim, C., Chen, K., Kim, J., and Que, L. (1997). Stereospecific Alkane Hydroxylation with H2O2 Catalyzed by an Iron(II)−Tris(2-pyridylmethyl)amine Complex. J. Am. Chem. Soc. *119*, 5964–5965. https://doi.org/10.1021/ja9642572.
40. Kim, H., Esser, L., Hossain, M.B., Xia, D., Yu, C.-A., Rizo, J., van der Helm, D., and Deisenhofer, J. (1999). Structure of Antimycin A1, a Specific Electron Transfer Inhibitor of Ubiquinol−Cytochrome c Oxidoreductase. J. Am. Chem. Soc. *121*, 4902–4903. https://doi.org/10.1021/ja990190h.
41. Chen, K., Costas, M., Kim, J., Tipton, A.K., and Que, L. (2002). Olefin Cis-Dihydroxylation versus Epoxidation by Non-Heme Iron Catalysts: Two Faces of an FeIII−OOH Coin. J. Am. Chem. Soc. *124*, 3026–3035. https://doi.org/10.1021/ja0120025.
42. Ho, R.Y.N., Roelfes, G., Feringa, B.L., and Que, L. (1999). Raman Evidence for a Weakened O−O Bond in Mononuclear Low-Spin Iron(III)−Hydroperoxides. J. Am. Chem. Soc. *121*, 264–265. https://doi.org/10.1021/ja982812p.
43. Lim, M.H., Rohde, J.-U., Stubna, A., Bukowski, M.R., Costas, M., Ho, R.Y.N., Münck, E., Nam, W., and Que, L. (2003). An $Fe^{IV}O$ complex of a tetradentate tripodal nonheme ligand. Proc. Natl. Acad. Sci. USA *100*, 3665–3670. https://doi.org/10.1073/pnas.0636830100.
44. Kim, J., Larka, E., Wilkinson, E.C., and Que, L. (1995). An Alkylperoxoiron(III) Intermediate and Its Role in the Oxidation of Aliphatic CH Bonds. Angew. Chem. Int. Ed. *34*, 2048–2051. https://doi.org/10.1002/anie.199520481.
45. Mairata i Payeras, A., Ho, R.Y.N., Fujita, M., and Que, L., Jr. (2004). The Reaction of [FeII(tpa)] with H2O2 in Acetonitrile and Acetone—Distinct Intermediates and Yet Similar Catalysis. Chem. Eur J. *10*, 4944–4953. https://doi.org/10.1002/chem.200400480.

46. Dharmaraja, A.T., and Chakrapani, H. (2014). A Small Molecule for Controlled Generation of Reactive Oxygen Species (ROS). Org. Lett. *16*, 398–401. https://doi.org/10.1021/ol403300a.
47. Zielonka, J., Vasquez-Vivar, J., and Kalyanaraman, B. (2008). Detection of 2-hydroxyethidium in cellular systems: a unique marker product of superoxide and hydroethidine. Nat. Protoc. *3*, 8–21. https://doi.org/10.1038/nprot.2007.473.
48. Kelkar, D.S., Ravikumar, G., Mehendale, N., Singh, S., Joshi, A., Sharma, A.K., Mhetre, A., Rajendran, A., Chakrapani, H., and Kamat, S.S. (2019). A chemical–genetic screen identifies ABHD12 as an oxidized-phosphatidylserine lipase. Nat. Chem. Biol. *15*, 169–178. https://doi.org/10.1038/s41589-018-0195-0.
49. Garcia-Irigoyen, O., Bovenga, F., Piglionica, M., Piccinin, E., Cariello, M., Arconzo, M., Peres, C., Corsetto, P.A., Rizzo, A.M., Ballanti, M., et al. (2022). Enterocyte superoxide dismutase 2 deletion drives obesity. iScience *25*, 103707. https://doi.org/10.1016/j.isci.2021.103707.
50. Pannu, V., Rida, P.C.G., Ogden, A., Clewley, R., Cheng, A., Karna, P., Lopus, M., Mishra, R.C., Zhou, J., and Aneja, R. (2012). Induction of robust de novo centrosome amplification, high-grade spindle multipolarity and metaphase catastrophe: a novel chemotherapeutic approach. Cell Death Dis. *3*, e346. https://doi.org/10.1038/cddis.2012.82.
51. Dixon, S.J., Lemberg, K.M., Lamprecht, M.R., Skouta, R., Zaitsev, E.M., Gleason, C.E., Patel, D.N., Bauer, A.J., Cantley, A.M., Yang, W.S., et al. (2012). Ferroptosis: An Iron-Dependent Form of Nonapoptotic Cell Death. Cell *149*, 1060–1072. https://doi.org/10.1016/j.cell.2012.03.042.
52. Palmer, G., Horgan, D.J., Tisdale, H., Singer, T.P., and Beinert, H. (1968). Studies on the respiratory chain-linked reduced nicotinamide adenine dinucleotide dehydrogenase. XIV. Location of the sites of inhibition of rotenone, barbiturates, and piericidin by means of electron paramagnetic resonance spectroscopy. J. Biol. Chem. *243*, 844–847.
53. Alexandre, A., and Lehninger, A.L. (1984). Bypasses of the antimycin a block of mitochondrial electron transport in relation to ubisemiquinone function. Biochim. Biophys. Acta *767*, 120–129. https://doi.org/10.1016/0005-2728(84)90086-0.
54. Yoshikawa, S., Shinzawa-Itoh, K., Nakashima, R., Yaono, R., Yamashita, E., Inoue, N., Yao, M., Fei, M.J., Libeu, C.P., Mizushima, T., et al. (1998). Redox-Coupled Crystal Structural Changes in Bovine Heart Cytochrome c Oxidase. Science (New York, N.Y.) *280*, 1723–1729. https://doi.org/10.1126/science.280.5370.1723.
55. Green, D.R., and Reed, J.C. (1998). Mitochondria and Apoptosis. Science (New York, N.Y.) *281*, 1309–1312. https://doi.org/10.1126/science.281.5381.1309.
56. Liu, X., Kim, C.N., Yang, J., Jemmerson, R., and Wang, X. (1996). Induction of apoptotic program in cell-free extracts: requirement for dATP and cytochrome c. Cell *86*, 147–157. https://doi.org/10.1016/s0092-8674(00)80085-9.
57. Wang, C., and Youle, R.J. (2009). The role of mitochondria in apoptosis. Annu. Rev. Genet. *43*, 95–118. https://doi.org/10.1146/annurev-genet-102108-134850.
58. Wang, Y., Wang, M., Djekidel, M.N., Chen, H., Liu, D., Alt, F.W., and Zhang, Y. (2021). eccDNAs are apoptotic products with high innate immunostimulatory activity. Nature *599*, 308–314. https://doi.org/10.1038/s41586-021-04009-w.
59. Belmokhtar, C.A., Hillion, J., and Ségal-Bendirdjian, E. (2001). Staurosporine induces apoptosis through both caspase-dependent and caspase-independent mechanisms. Oncogene *20*, 3354–3362. https://doi.org/10.1038/sj.onc.1204436.
60. Caserta, T.M., Smith, A.N., Gultice, A.D., Reedy, M.A., and Brown, T.L. (2003). Q-VD-OPh, a broad spectrum caspase inhibitor with potent antiapoptotic properties. Apoptosis *8*, 345–352. https://doi.org/10.1023/a:1024116916932.
61. Nwosu, Z.C., Battello, N., Rothley, M., Piorońska, W., Sitek, B., Ebert, M.P., Hofmann, U., Sleeman, J., Wölfl, S., Meyer, C., et al. (2018). Liver cancer cell lines distinctly mimic the metabolic gene expression pattern of the corresponding human tumours. J. Exp. Clin. Cancer Res. *37*, 211. https://doi.org/10.1186/s13046-018-0872-6.
62. Shi, J., Wang, X., Lyu, L., Jiang, H., and Zhu, H.-J. (2018). Comparison of protein expression between human livers and the hepatic cell lines HepG2, Hep3B, and Huh7 using SWATH and MRM-HR proteomics: Focusing on drug-metabolizing enzymes. Drug Metab. Pharmacokinet. *33*, 133–140. https://doi.org/10.1016/j.dmpk.2018.03.003.
63. Gunn, P.J., Green, C.J., Pramfalk, C., and Hodson, L. (2017). In vitro cellular models of human hepatic fatty acid metabolism: differences between Huh7 and HepG2 cell lines in human and fetal bovine culturing serum. Physiol. Rep. *5*, e13532. https://doi.org/10.14814/phy2.13532.
64. Raza, K., Kumar, N., Misra, C., Kaushik, L., Guru, S.K., Kumar, P., Malik, R., Bhushan, S., and Katare, O.P. (2016). Dextran-PLGA-loaded docetaxel micelles with enhanced cytotoxicity and better pharmacokinetic profile. Int. J. Biol. Macromol. *88*, 206–212. https://doi.org/10.1016/j.ijbiomac.2016.03.064.
65. Xu, Z., Zhu, S., Wang, M., Li, Y., Shi, P., and Huang, X. (2015). Delivery of Paclitaxel Using PEGylated Graphene Oxide as a Nanocarrier. ACS Appl. Mater. Interfaces *7*, 1355–1363. https://doi.org/10.1021/am507798d.
66. Misra, S.K., Wu, Z., Ostadhossein, F., Ye, M., Boateng, K., Schulten, K., Tajkhorshid, E., and Pan, D. (2019). Pro-Nifuroxazide Self-Assembly Leads to Triggerable Nanomedicine for Anti-cancer Therapy. ACS Appl. Mater. Interfaces *11*, 18074–18089. https://doi.org/10.1021/acsami.9b01343.
67. Vacca, A., Bruno, M., Boccarelli, A., Coluccia, M., Ribatti, D., Bergamo, A., Garbisa, S., Sartor, L., and Sava, G. (2002). Inhibition of endothelial cell functions and of angiogenesis by the metastasis inhibitor NAMI-A. Br. J. Cancer *86*, 993–998. https://doi.org/10.1038/sj.bjc.6600176.
68. Frausin, F., Scarcia, V., Cocchietto, M., Furlani, A., Serli, B., Alessio, E., and Sava, G. (2005). Free Exchange across Cells, and Echistatin-Sensitive Membrane Target for the Metastasis Inhibitor NAMI-A (Imidazolium trans-Imidazole Dimethyl Sulfoxide Tetrachlororuthenate) on KB Tumor Cells. J. Pharmacol. Exp. Ther. *313*, 227–233. https://doi.org/10.1124/jpet.104.078352.
69. Sava, G., Frausin, F., Cocchietto, M., Vita, F., Podda, E., Spessotto, P., Furlani, A., Scarcia, V., and Zabucchi, G. (2004). Actin-dependent tumour cell adhesion after short-term exposure to the antimetastasis ruthenium complex NAMI-A. Eur. J. Cancer *40*, 1383–1396. https://doi.org/10.1016/j.ejca.2004.01.034.
70. Garzon, F.T., Berger, M.R., Keppler, B.K., and Schmähl, D. (1987). Comparative antitumor activity of ruthenium derivatives with 5′-deoxy-5-fluorouridine in chemically induced colorectal tumors in SD rats. Cancer Chemother. Pharmacol. *19*, 347–349. https://doi.org/10.1007/BF00261487.
71. Keppler, B.K., and Rupp, W. (1986). Antitumor activity of imidazolium-bisimidazole-tetrachlororuthenate (III). J. Cancer Res. Clin. Oncol. *111*, 166–168. https://doi.org/10.1007/BF00400758.
72. Romero-Canelón, I., and Sadler, P.J. (2013). Next-Generation Metal Anticancer Complexes: Multitargeting via Redox Modulation. Inorg. Chem. *52*, 12276–12291. https://doi.org/10.1021/ic400835n.
73. Yellol, J., Pérez, S.A., Buceta, A., Yellol, G., Donaire, A., Szumlas, P., Bednarski, P.J., Makhloufi, G., Janiak, C., Espinosa, A., and Ruiz, J. (2015). Novel C,N-Cyclometalated Benzimidazole Ruthenium(II) and Iridium(III) Complexes as Antitumor and Antiangiogenic Agents: A Structure-Activity Relationship Study. J. Med. Chem. *58*, 7310–7327. https://doi.org/10.1021/acs.jmedchem.5b01194.
74. Gill, M.R., Harun, S.N., Halder, S., Boghozian, R.A., Ramadan, K., Ahmad, H., and Vallis, K.A. (2016). A ruthenium polypyridyl intercalator stalls DNA replication forks, radiosensitizes human cancer cells and is enhanced by Chk1 inhibition. Sci. Rep. *6*, 31973. https://doi.org/10.1038/srep31973.
75. Zeng, L., Gupta, P., Chen, Y., Wang, E., Ji, L., Chao, H., and Chen, Z.-S. (2017). The development of anticancer ruthenium(ii) complexes: from single molecule compounds to nanomaterials. Chem. Soc. Rev. *46*, 5771–5804. https://doi.org/10.1039/c7cs00195a.
76. Lin, Y., Choksi, S., Shen, H.M., Yang, Q.F., Hur, G.M., Kim, Y.S., Tran, J.H., Nedospasov, S.A., and Liu, Z.G. (2004). Tumor necrosis factor-induced nonapoptotic cell death requires receptor-interacting protein-mediated cellular reactive oxygen species accumulation. J. Biol. Chem. *279*, 10822–10828. https://doi.org/10.1074/jbc.M313141200.
77. Weinlich, R., Oberst, A., Beere, H.M., and Green, D.R. (2017). Necroptosis in development, inflammation and disease. Nat. Rev. Mol. Cell Biol. *18*, 127–136. https://doi.org/10.1038/nrm.2016.149.
78. Lim, M.H., Rohde, J.U., Stubna, A., Bukowski, M.R., Costas, M., Ho, R.Y.N., Munck, E., Nam, W., and Que, L., Jr. (2003). An FeIV=O complex of a tetradentate tripodal nonheme ligand. Proc. Natl. Acad. Sci. USA *100*, 3665–3670. https://doi.org/10.1073/pnas.0636830100.
79. Chan, S.L.-F., Lam, T.L., Yang, C., Yan, S.-C., and Cheng, N.M. (2015). A robust and efficient cobalt molecular catalyst for CO2 reduction. Chem. Commun. *51*, 7799–7801. https://doi.org/10.1039/C5CC00566C.
80. Kunishita, A., Kubo, M., Ishimaru, H., Ogura, T., Sugimoto, H., and Itoh, S. (2008). H2O2-Reactivity of Copper(II) Complexes Supported by Tris[(pyridin-2-yl)methyl]amine Ligands with 6-Phenyl Substituents. Inorg.

Chem. *47*, 12032–12039. https://doi.org/10.1021/ic801568g.

81. Dolomanov, O.V., Bourhis, L.J., Gildea, R.J., Howard, J.A.K., and Puschmann, H. (2009). OLEX2: a complete structure solution, refinement and analysis program. J.App. Cryst. *42*, 339–341. https://doi.org/10.1107/S0021889808042726.
82. Sheldrick, G.M. (2015). SHELXT - Integrated space-group and crystal-structure determination. Acta Cryst. A *71*, 3–8. https://doi.org/10.1107/S2053273314026370.
83. Sheldrick, G.M. (2015). Crystal structure refinement with SHELXL. Acta Cryst. C *71*, 3–8. https://doi.org/10.1107/S2053229614024218.
84. Samimi, H., Sohi, A.N., Irani, S., Arefian, E., Mahdiannasser, M., Fallah, P., and Haghpanah, V. (2021). Alginate-based 3D cell culture technique to evaluate the half-maximal inhibitory concentration: an in vitro model of anticancer drug study for anaplastic thyroid carcinoma. Thyroid Res. *14*, 27. https://doi.org/10.1186/s13044-021-00118-w.
85. Xu, X.X., Liu, C., Liu, Y., Yang, L., Li, N., Guo, X., Sun, G.W., and Ma, X.J. (2014). Enrichment of cancer stem cell-like cells by culture in alginate gel beads. J. Biotechnol. *177*, 1–12. https://doi.org/10.1016/j.jbiotec.2014.02.016.
86. Monaco, I., Camorani, S., Colecchia, D., Locatelli, E., Calandro, P., Oudin, A., Niclou, S., Arra, C., Chiariello, M., Cerchia, L., and Comes Franchini, M. (2017). Aptamer Functionalization of Nanosystems for Glioblastoma Targeting through the Blood–Brain Barrier. J. Med. Chem. *60*, 4510–4516. https://doi.org/10.1021/acs.jmedchem.7b00527.

STAR★METHODS

KEY RESOURCES TABLE

REAGENT or RESOURCE	SOURCE	IDENTIFIER
Antibodies		
β-tubulin	ACell Signaling Technology	Cat # #2146; AB_2210545
Cytochrome *c* (136F3) Rabbit mAb	Cell Signaling Technology	Cat# 4280T; AB_10695410
Caspase 3 Recombinant Rabbit Monoclonal Antibody	Thermo Fisher Scientific	Cat # 700182; AB_2532293
Caspase 3 (Cleaved Asp175) Polyclonal Antibody	Thermo Fisher Scientific	Cat # PA5-114687; AB_2899323
PARP1 Recombinant Rabbit Monoclonal Antibody	Thermo Fisher Scientific	Cat # MA5-41125; AB_2898879
Alexa 488-conjugated Goat anti-rabbit antibody	Thermo Fisher Scientific	Cat# A-11008; AB_143165
Chemicals, peptides, and recombinant proteins		
Annexin - V	Alexa flour 488 – Thermo	Cat # A13201
CellTiter-Glo® 2.0	Promega	Cat #G9241
Trypsin-0.25% Trypsin-EDTA –	Gibco-Thermo Fisher Scientific	Cat # 25200056
DMEM media high glucose	Gibco-Thermo Fisher Scientific	Cat # 11965092
Doxorubicin	Sigma Aldrich	Cat # 44583
Cisplatin	Alfa Aeser	Cat # 10471
Tetramethyl rhodamine, methyl ester percholate	Thermo Fisher Scientific	Cat #T668
Hoechst 33342 Solution (20 mM)	Thermo Fisher Scientific	Cat # 62249
H2DCFDA	Thermo Fisher Scientific	Cat #D399
Q-VD-OPh hydrate	Adooq Bioscience	Cat # A14915
Necrostatin-1	Adooq Bioscience	Cat # A11973
Ferrostatin-1	Adooq Bioscience	Cat # A13247
Sodium Azide	Sigma Aldrich	Cat #S8032
Rotenone	Adooq Bioscience	Cat # A10811
Antimycin A	AKScientific Inc	Cat # 0974BB
Dimethylsulfoxide-d_6	Synmr Chemicals Pvt Ltd, Bangalore India	Cat #D30
D2O	https://www.sigmaaldrich.com/	Cat # 151882
N-acetylcysteine	https://www.sigmaaldrich.com/	Cat# A0737
phosphate buffer-saline	https://www.thermofisher.com/	Cat# 70011069
Acetonitrile (HPLC)	https://www.sigmaaldrich.com/	Cat# 34998
Trifluroaceitic acid		Cat# 302031
Potassium Phosphate tribasic		Cat# P5629
Tris(2-carboxyethyl)phosphine hydrochloride		Cat# 75259
DL-Dithiothreitol		Cat# D0632
MitoSOX Green	Thermo Fisher Scientific	Cat#M36008
Amplex Red	Thermo Fisher Scientific	Cat#A12222
Horse Radish Peroxaidase	Sigma Aldrich	Cat#P8375-1KU

(*Continued on next page*)

Continued

REAGENT or RESOURCE	SOURCE	IDENTIFIER
Catalse	Sigma Aldrich	Cat#C40
Superoxide dismutase	Sigma Aldrich	Cat#S5395
Dihydroethidium	Sigma Aldrich	Cat#309800
Propidium iodide	Sigma Aldrich	Cat#537059
Thiobarbituric acid	Glr innovations	Cat#504-17-6
Experimental models: Cell lines		
HEK293 Cells	Cells Repository, National Center for Cell Sciences (NCCS)-Pune, India	Cat# HEK293
A549 lung cancer cells		Cat # A549
H9C2, Heart cells		Cat #H9c2(2-1)
A375, Melanoma cell		Cat # A375
U87MG, Glioblastoma		Cat #U87MG
HCT116, Colon cancer cells		Cat # HCT116
PC-3, Prostate cancer cells		Cat # PC-3
MDA-MB-231, Triple-negative breast cancer cells		Cat # MDA-MB-231
MCF7, breast cancer cells		Cat # MCF7
RPMI8226, myeloma cells		Cat # RPMI8226
U2OS, Osteosarcoma cells	Gift from Prof Nitin Mohan IIT Kanpur	
Huh7 cell	Gift from Prof Nitin Mohan IIT Kanpur	
Software and algorithms		
Gel Imaging	ChemiDoc™ Touch Imaging System	Bio-Rad
High-performance liquid chromatography (HPLC)	Agilent	Agilent Tech
Fluorimetric, luminometric and spectrophotometric measurements	Promegapc-GloMax®	Promega
Graphpad Prsim 9.4.0	Graphpad Prsim	https://www.graphpad.com/
ChemDraw Professional 21.0	PerkinElmer	https://www.perkinelmer.com/category/chemdraw
Others		
PVDF membrane	https://www.thermofisher.com/	Cat # 88520

RESOURCE AVAILABILITY

Lead contact

For example, "Further information and requests for resources should be directed to and will be fulfilled by the lead contact, Dharmaraja Allimuthu (atdharma@iitk.ac.in)."

Materials availability

All materials generated in this study are available from the lead contact without restriction.

Data and code availability

- All datasets reported in this work are available from the lead contact upon request.
- This paper does not report original code.
- Any additional information required to reanalyse the data reported in this paper is available from the lead contact upon request.
- All data generated or analyzed during this study are included in the manuscript and supporting files.

EXPERIMENTAL MODEL AND STUDY PARTICIPANT DETAILS

Cell lines

Cell lines used were cultured in either DMEM or RPMI media were supplemented with 10% FBS (Fetal Bovine Serum- Gibco) and 1% PenStrep (Pencillin Streptomycin- Gibco) at 37°C and 5% CO_2 atmosphere.

RPMI Media: A549: Lung carcinoma epithelial cells; PC3: Prostate cancer; RPMI 8226: B lymphocytes; Jurkat J6: Acute T cell Leukemia; MCF7: Breast cancer MDA-MB-231; Triple negative breast cancer.

DEME Media: HepG2 & Huh-7: Hepatocellular carcinoma; U2OS: Osteosarcoma; A375: Melanoma; HCT-116: Colon cancer; U87MG: Glioblastoma.

METHOD DETAILS

General information

All chemicals and reagents were obtained from commercial sources and were used as received. HPLC grade solvents, H_2O and CH_3CN from Merck were used in spectroscopic studies. Elemental analyses (C, H, N) were obtained using PerkinElmer CHNS/O 2400 series II Analyser. IR spectrum was recorded using Zn-Se pellets with a ECO-ATR spectrometer (Bruker Alpha II). Agilent 8453 diode-array spectrophotometer was used to record UV/Vis absorption spectra and conduct kinetic experiments spectrophotometrically in 1 cm quartz cells (λ = 190–1100 nm range). The ^{1}H and ^{13}C NMR spectra were obtained using JEOL JNM LA 400 (400 MHz) NMR spectrometer and JEOL JNM LA 500 (500 MHz) and tetramethylsilane (TMS) used as the internal standard to record NMR. Elemental Analysis was recorded using Elementar Unicube v1.1.6 instrument. Bruker EMX 1444 spectrometer with the temperature controller was employed to record the X-band EPR data at 120 K. Simulation of EPR Spectrum was carried out by Bruker WINEPR SimFonia software. The spectrometer was calibrated using 3-bwasdiphenylene-2-phenylallyl (BDPA) as X-Band EPR standard.

Cyclic Voltammetry experiments were carried out at room temperature using the CH instrument's Electrochemical Analyzer M-600B series. A three-electrode system was used where glassy carbon was used as a working electrode, Pt wire as an auxiliary electrode, and the aqueous Ag/AgCl the reference electrode. The solutions used were 1 mM of complex and 120 mM of supporting electrolyte tetra-*n*-butylammonium perchlorate in acetonitrile and potassium nitrate in water, respectively.

Compounds IITK4002,[78] IITK4005,[79] IITK4006[35,80] and IITK4007[80] were synthesized as per literature reports and the characterization data were in agreement with the reported ones.

X-ray crystallography

Single crystal of suitable dimensions was used for data collection. Diffraction intensities were collected on a Brucker APEX-II CCD diffractometer, with graphite-monochromated Mo Kα (0.71073 Å) radiation at 100(2) K. Data were corrected for Lorentz and polarization effects; empirical absorption corrections (SADABS v 2.10) were applied. Using Olex2,[81] the structures were solved by ShelXT[82] structure solution program using Intrinsic Phasing and refined with the ShelXL[83] refinement package using Least Squares minimization. The position of the hydrogen atoms was calculated by assuming ideal geometries but not refined. All non-hydrogen atoms were refined with anisotropic thermal parameters by full-matrix least-squares procedures on F2. CCDC 2284859, 2206145, and 2206291 contain the supplementary crystallographic data for IITK4003, IITK4004, and IITK4008, respectively. This data can be obtained free of charge from the Cambridge Crystallographic Data Center via www.ccdc.cam.ac.uk.

Synthesis and characterization

Synthesis of 2-(chloromethyl)-1-methyl-1H-benzo[d]imidazole

N-methylbenzene-1,2-diamine (3 g, 15.4 mmol) was dissolved in 32 mL of 6 N HCl followed by the addition of 2-chloroacetic acid (2.168 g, 23.07 mmol) in a round-bottom flask. The reaction vessel was placed 80°C for 8 h and cooled down to room temperature. Then, the reaction mixture was placed on an ice bath under continuous stirring and an aqueous ammonia solution was added dropwise to neutralize the excess acid. A brown precipitate appeared after neutralisation that was filtered over G2 frit and washed with cold water. The solid was kept for drying overnight in a vacuum desiccator. The crude was purified by column chromatography over neutral alumina, using chloroform as eluting solvent. The crude product obtained after column purification was redissolved in CHCl3 and excess hexane poured to bring the compounds to its saturation solubility. The slow evaporation of the solution gave white crystalline product in 2 days. Yield: 1.47 g, 52%. 1H NMR (400 MHz, CDCl3): δ (ppm) 7.76–7.75 (d, 1H, J = 7.44 Hz), 7.35–7.27 (m, 3H), 4.83 (s, 2H), 3.84 (s, 3H). 13C NMR (CDCl3, 100 MHz): δ (ppm) 149.10, 142.05, 136.23, 123.75, 122.80, 120.23, 109.61, 36.90, 30.34.

Synthesis of N^1-benzyl-N^1, N^2, N^2-tris((1-methyl-1H-benzo[d]imidazol-2-yl)methyl)ethane-1,2-diamine (IITK4001)

To a solution of 2-(chloromethyl)-1-methyl-1H-benzo[*d*]imidazole (1.5 g, 8.33 mmol) in 15 mL of water, N1-benzylethane-1,2-diamine (424.3 μL, 2.7 mmol) and aqueous NaOH solution (0.33 g, 8.33 mmol) were slowly added sequentially, over a period of an hour. The resulting mixture was stirred at room temperature for 7 days and complete consumption of the starting material was observed using thin-layer chromatography (TLC) analysis. Then, the reaction mixture was extracted with methylene chloride (3 × 25 mL) and the combined organic phases were dried over Na2SO4.The solvent was evaporated under reduced pressure to obtain pure product as a while solid. Yield: 1 g (70%).

Characterization: 1H NMR (400 MHz, CDCl3) δ (ppm) 7.70–7.66 (m, 3H), 7.24–7.22 (m, 6H), 7.16 (d, 2H, J = 4 Hz), 7.16–7.14 (m, 2H), 7.13 (d, 4H, J = 1.44 Hz), 3.90 (s, 4H), 3.79 (s, 2H), 3.58 (s, 2H), 3.44 (s, 3H), 3.36 (s, 6H), 2.89 (t, 2H, J = 6.28 Hz), 2.73 (t, 2H, J = 6.32 Hz). 13C NMR (100 MHz, CDCl3) δ (ppm) 151.64, 151.17, 135.93, 129.39, 128.35, 127.47, 122.97, 122.34, 118.56, 119.25, 109.42, 109.33, 59.61, 52.62, 51.76, 51.49, 51.35, 30.00, 29.68.

Synthesis of $[Fe^{III}(IITK4001)(OCH_3)](ClO_4)_2$ (IITK4003)

In a round-bottom flask [FeII(H2O)6](ClO4)2 (62.28 mg, 0.171 mmol) was dissolved in the minimum amount of acetonitrile. To this equimolar amount of BnTBEN (100 mg, 0.171 mmol) solution in CH3OH was added dropwise. The reaction mixture was stirred for 3 h at room temperature and thenexcess diethyl ether poured in the reaction mixture to get red precipitate. The solid was washed thrice with diethyl ether and dried under reduced pressure to obtain the pure product as a red-coloured precipitate. Yield: 110 mg (71%). Single crystals suitable for X-ray analysis were obtained by the slow vapor diffusion of diethyl ether into the 1:1 acetonitrile:CH3OH solution of IITK4003 at room temperature. UV Vis: 245 nm (ε = 42480 M-1 cm-1), 272 nm (ε = 52800 M-1 cm-1), 280 nm (ε = 50400 M-1 cm-1) and a broad band at 376 nm (ε = 8400 M-1 cm-1). Anal. Calc. for $C_{37}H_{41}Cl_2FeN_8O_9$: C 51.17, H 4.76, *N* 12.90. Found: C 51.59, H 4.78, *N* 13.37.

Synthesis of $[Fe^{III}{}_2(IITK4002)_2(\mu\text{-}O)(H_2O)_2]](ClO_4)_4$ (IITK4004)

An instant red colored solution was obtained by combining 2 mL acetonitrile solution of [FeII(H2O)6](ClO4)2 (199 mg, 0.55 mmol) to 2 mL acetonitrile solution of IITK4002 (159.5 mg, 0.55 mmol) at room temperature. The reaction mixture was stirred for 3 h and then half of the volume of solvent was removed under reduced pressure. To this reaction mixture, = excess diethyl ether was added and obtained a red-coloured precipitate. Then, this solid of IITK4004 was washed with diethyl ether (3 × 25 mL) and dried under reduced pressure before crystallization to obtain pure product. Crystallization was accomplished through diethyl ether vapor diffusion into an acetonitrile solution of IITK4004. Red-coloured shiny needle-like crystals suitable for X-ray analyses were obtained in 2 days at 25°C. Yield: 150 mg (24%). Elemental Analysis: Calculated for $[Fe^{III}{}_2(IITK4002)_2(\mu\text{-}O)(H_2O)_2](ClO_4)_4$: C 37.85%, H 3.53%, *N* 9.78%. Found, C 37.11%, H 3.36%, *N* 9.52%.

Synthesis of $[Zn^{II}(IITK4002)(H_2O)](CF_3SO_3)_2$ (IITK4008)

To a solution of IITK4002 (50.5 mg, 174 μmol) in CH3CN (2 mL), [ZnII(H2O)6](CF3SO3)2 (63.2 mg, 174 μmol) solution in CH3CN (4 mL) was added at room temperature. After stirring the reaction mixture for 3 h, the solvent was removed under reduced pressure to obtain IITK4008 as a white solid. Then, the recrystallization of IITK4008 carried out through diethyl ether vapor diffusion into acetonitrile solution at room temperature to obtain white crystals of $[Zn^{II}(IITK4002)(H_2O)](CF_3SO_3)_2$ complex suitable for X-ray analyses. Yield: 72 mg (62%).

HPLC for purity analysis

High-performance liquid chromatography (HPLC) was performed on an Agilent 1260 infinity machine model with a ZORBAX SB-C-18 (150 × 4.6 mm, 5 μm)/Poroshell-120 EC-C18 (150 × 2 mm, 2.7 μm) reverse phase columns and diode array detector (detection wavelength 496, 258 and 315 nm). The stock solutions of all the compounds (10 mM) were prepared in acetonitrile (HPLC Grade obtained from FINAR) and analysis were performed at 0.8 mM final concentration in MeCN. A gradient elution protocol was used with a mixture of MeCN and water containing 0.1% trifluoroacetic acid with the following ratio: 0–4 min: 30% acetonitrile in water; 4 to 6 min: 60% acetonitrile in water; 6 to 8 min: 100% acetonitrile; and 8 to 10 min: 30% MeCN in water.

Cell viability assessment: General protocol

Cells were cultured in a T75 filter flasks (ThermoFisher) until they attained 70–80% confluency and trypsinized with 4 mL of 0.25% Trypsin-EDTA(Gibco). Then, the cells were counted, seeded in a 384 well plate(500 cells/well in 75 μL of media) and allowed to attach for 24 h under standard conditions (37°C, 5% CO_2). After 24 h, the cells were treated with our test compounds in triplicate, DMSO (0.1%, SRL) served as negative control, and the positive controls used were doxorubicin (0.5 μM, sigma) and cisplatin (5 μM, Alfa-Aesar). After 72 h of treatment, the media was discarded and replaced with assay reagent (CellTiter-Glo (CTG) or resazurin) to quantify the viable cell counts using either CTG assay (CTG, Promega) or resazurin assay. CTG assay: Briefly, CTG (30 μL of 1x (CTG from Promega was 3-fold diluted with 1X PBS)) was added to the wells and the plate was placed dark at room temperature for 5 min. The, the plate was spun down for a minute at 1000 RPM before recording luminescence readings using a multimode plate reader. Resazurin assay: Resazurin solution (75 μL of 2 μg/mL in phosphate buffered saline, PBS)) was added to the wells and incubated under standard conditions for 6 h before measuring fluorescence emission (λ_{ex} 520 nm; λ_{em} 580 nm) using a multimode plate reader (BioTek-CYTATION 5- imaging reader). The percentage cell viability was calculated with respect to DMSO. Graphs were plotted using the Graphpad Prism 9.0 software.

Concentrations of compounds used in the cell viability assays

For the 2-dose screening, 20 μM and 5 μM of the ligands were taken and CTG assay was used., For a dose-dependent evaluation, we used an eight-point-three-fold-dilution series with concentrations ranging from 100 μM to 0.04 μM using CTG (all cancer cell lines) and resazurin (U2OS cells) assays. For combination assay: Metal salts-20 μM ($Fe(ClO_4)_2$, $Zn(OTf)2$, $CoCl_2$, $Ni(ClO_4)_2$), deferoxamine-2 μM, H_2O_2-150 μM, ^{t}BuOOH-30 μM, *N*-acetylcysteine-0.5 mM, α-tocopherol −100 μM, Butathionine sulfoximine-25 μM, QVD-OPh-10 μM, RSL3-0.5 μM, ferrostatin-1-10 μM, necrostatin-1-10 μM were used.

Mitochondrial ROS and membrane potential assessment

In a 96-well plate, 25000 cells in 200 μL DMEM media per well were seeded and incubated for 24 h under standard conditions. Then, the cells were treated with DMSO (0.02%), or compounds (IITK4003- 20 μM, IITK4004-20 μM, H_2O_2 - 150 μM, JCHD- 150 μM, IITK4003 (20 μM) + H_2O_2 (150 μM), IITK4004 (20 μM)+ H_2O_2 (150 μM) for 90 min. After the treatment, the media was removed and the cells were washed with PBS (ax, 100 μL) and placed with 50 μL of media containing Tetramethyl rhodamine, methyl ester percholate (TMRM, 30 nM), Hoechst 33342 (1 μg/mL) and MitoSOX green (1 μM) for 30 min treatment at 37°C. Post incubation, the cells were washed with PBS (1x, 100 μL) for twice and the images were captured using fluorescent microscope (Bio-Rad ZOE fluorescent cell imager) in the green channel (λ_{ex} 480 nm; λ_{em} 517 nm) for MitoSOX green, red channel (λ_{ex} 556 nm; λ_{em} 615 nm) for TMRM, blue channel (λ_{ex} 355 nm; λ_{em} 433 nm) for Hoechst. Images colocalizations were performed using ImageJ software.

ROS quantification by using DCFDA

Protocols for seeding cells and compounds treatment were followed as mentioned in the above experiment for mitochondrial ROS assessment. The compounds used in this experiment for the treatment were DMSO (0.02%), tert-BuOOH (60 μM in U2OS and 100 μM in Huh-7), H_2O_2 (150 μM, NAC (0.5 mM), IITK compounds at 20 μM (IITK4001, IITK4002, IITK4003 and IITK4004) and their combination with ROS modulators at the inducated concentrations. After the treatment, 2′,7′-Dichlorofluorescein 3′,6′-diacetate (2 μM H_2-DCFDA) and incubated for 5 min at 37°C. Then, the media was removed, cells were washed with PBS (100 μL each) for twice before capturing image using a fluorescent microscope (Bio-Rad ZOE fluorescent cell imager) in the green channel (λ_{ex} 480 nm; λ_{em} 517 nm).

Cellular ATP quantification

A calibration curve for ATP standard (Sigma) was generated for 8-copncentrations of ATP at a 4-fold dilution starting from 100 μM (to 0.006 μM) in triplicate. To the ATP solution (50 μL) in a white bottom 96 well plate, CTG reagent (25 μL of 3x) was added, and the luminescence was recorded instantly, and this was used for quantifying cellular ATP levels. Next, cells (20,000 per well in 200 μL DMEM) were seeded in white flat bottom 96 well plates and incubated under standard conditions for 24 h before treating with our compounds (IITK4001 & IITK4003 at 10, 30, 50 μM and IITK4003 & IIYK4004 at 1, 10, 30 μM) and controls (Antimycin A (0.2 μM), rotenone (0.3 μM), NaN_3 (1 mM). After incubation, the media was replaced with 75 μL of 1X CTG reagent, incubated at room temperature for 10 min before recording luminescence readings.

Amplex red assay

A calibration curve for H_2O_2 standard was generated for 8-copncentrations of ATP at a 3-fold dilution starting from 5 μM (to 2 nM) in triplicate in a 96-well plate. To the H2O2 standard plate, Amplex Red mix (Amplex red, 50 μL, 50 μM and HorseRadish Peroxidase enzyme, HRP, 0.1 U/mL in 0.5X PBS) was added and the fluorescence emission was recorded at λ_{ex} 530 nm; λ_{em} 590 nm. Then, Huh-7 cells were seeded in a clear bottom 96 well plate (20000 cells in 50 μL 0.5x PBS per well) and treated immediately with our compounds (IITK4003 and IITK4004 (20, 10, and 5 μM) alone or in combination with H_2O_2 (5 μM). All the conditions are further treated with catalase (100 U/mL) and superoxide dismutase (4 U/mL) independently. Post treatment, cells were incubated for 1 h under standard conditions (5% CO_2, 37°C) and Amplex Red reagent mix was added before recording fluorescence emission (λ_{ex} 530 nm; λ_{em} 590 nm).

Dihydroethidine (DHE) oxidation assay

For the DHE assay, Huh-7 cells were plated in a96-well plate (10000 cells per well in 50 μL 1X PBS) and treated immediately with IITK4003 and IITK4004 (20, 10 and 5 μM), H_2O_2 (5 μM) alone in combination.[46,47] All the conditions are further treated with catalase (100 U/mL) and superoxide dismutase (4 U/mL) independently and incubated for 1 h. Post treatment,the DHE dye (50 μM final concentration) was added to all the wells and incubated again for 1 h, then the fluorescence emission was recorded at λ_{ex} 510 nm; λ_{em} 610 nm.

Propidium iodide staining and annexin-V immunostaining

In a 96-well plate, cells were seeded at a density of 25000 cells per well in 200 μL DMEM medium and incubated under standard conditions for 24 h. Post incubation, the cells were treated for 12 h with DMSO (0.02%) or our compounds (IITK4001- = IITK4004 (20 μM)) alone or in combination with staurosporine (250 nM), QVD-OPh (10 μM), necrostatin-1 (10 μM). Propidium iodide staining: After incubation, propidium iodide (5 μg/mL in DMEM) was added to the cells and incubated for 20 min before capturing images using a fluorescent microscope in the red channel (λ_{ex} 556 nm; λ_{em} 615 nm).

Annexin-V immunostaining: Post incubation, cells were washed with PBS (100 μL) and added with Annexin-V (2 μL of Alexa flour 488 – ThermoFisher in 100 μL of annexin binding buffer: 10 mM HEPES, 150 mM NaCl, 2.5 mM $CaCl_2$). Then, the plate was incubated for 6 h under standard conditions before imaging using a fluorescent microscope in the green channel (λ_{ex} 480 nm; λ_{em} 417 nm).

Western blotting

In a 6-well plate, 100,000 cells/well were seeded and incubated under standard conditions for 24 h. Then, the cells were treated for 4 and 8 h with our compounds (IITK4001-IITK4004, 30 μM) and 6 h with staurosporine (100 nM) at 37°C. Post treatment, the cells were washed with ice-cold PBS (2 mL) and scraped after the addtion of protease phosphatase inhibitor cocktail (1x, 60 μL ThermoFisher). Then, the cells were lysed using probe sonicator and centrifuged at 20,000 g for 45 min at 4°C to clarify the cell debris and collected the supernatant protein solution.

This was subjected to Bradford assay for protein quantification and for the quantity normalization. From each condition, 20 μg of protein was resolved on a 4–12% polyacrylamide gel for 90 min at 130 V and the proteins were transferred to a PVDF membrane (Bio-rad) for 12 h at 40 V, 4°C by in a transfer buffer (Tris base-glycine in 20% methanol water). The membrane was washed for 10 min with distilled water and trimmed according to the molecular weight of desired protein. Then, the membranes were blocked for 1 h with 5% skimmed milk in 1X TBST and washed thrice with 1X TBST (10 min each). Next, the membranes were incubated with primary antibodies in 1% skimmed milk with 1X TBST, i.e., β-tubulin (Anti-Rabbit-1:500 dilution-Abgenex), caspase-3 (Anti-Rabbit-1:1000 dilution), cleaved caspase-3 (Anti-Rabbit-1:1000 dilution) and cleaved PARP-1 (Anti-Rabbit-1:1000 dilution) antibodies for overnight at 4°C [caspase and PARP antibodies were gifted by Dr. Jayandhran and Dr. Bushra Ateeq of IIT Kanpur]. After incubation with primary antibody, the membranes were washed thrice with 1X TBST (10 min each). Then, the membranes were incubated with anti-rabbit secondary antibody (1:5000 dilution) in 1% skimmed milk for 1 h at room temperature and washed thrice with 1X TBST (10 min each). Finally, the blots were developed using luminol (250 mM) and *p*-coumaric acid (90 mM) in 50% H_2O_2. The blots were visualized by using chemidoc instrument's chemiluminescence filter.

TBARS assay

Malondialdehyde (MDA) tetrabutylammonium salt (sigma) calibration curve was generated for a four-concentration of 2-fold dilution series starting from 2.5 μM (to 0.312) in 2.5% TCA in water in triplicate. To these, 0.67% TBA (100 μL) was added and heated at 95°C for 30 min and allowed to cool down to room temperature before recording fluorescence emission at λ_{ex} 530 nm; λ_{em} 550 nm. For lipid peroxidation assay in Huh-7 cells, 0.35 million cells per well were seeded in a clear bottom 12 well plate and incubated for 24 h before the treatment with indicated conditions (DMSO, IITK4001-IITK4004 (20 μM) and Diethyl maleate (4 mM) for 6 h at 37°C. Then, the cells were washed with ice-cold PBS and scrapped by adding 2.5% trichloroacetic acid (200 μL) in water and centrifuged for 15 min at 13,000g. Next, the supernatant was collected and 15% TCA in water (200 μL) and 0.67% thiobarbituric acid (TBA, 500 μL in water) were added, mixed (vortexed) and heated at 95°C for 30 min before allowing to cool down to room temperature. Then, n-butanol (500 μL) was added to all the samples and allowed the separation of the aqueous and organic phases, and the organic layer was collected (200 μL/well in a 96-well plate) for recording the fluorescence emission at λ_{ex} 530 nm; λ_{em} 550 nm.

Pγ-H2AX immunostaining

For Pγ-H2AX immunostaining experiment in Huh-7 cells, 25000 cells per well were seeded in clear bottom 12 well plate and incubated at 37°C for 24 h. Then, the cells were treated with with DMSO or our compounds (IITK4001-IITK4004 (20 μM) and doxorubicin (1 μM) for 2 h and washed with ice-cold PBS (200 μL) before fixing with 4% formaldehyde (100 μL in water) for 15 min at room temperature. Then, ice-cold 100% methanol (100 μL) was added to the cells and incubated at −20°C for 10 min and again washed with ice-cold PBS (200 μL each) thrice. Next, Pγ-H2AX was diluted in 1:50 ratio using antibody dilution buffer (1% BSA in 1X PBS) and 50 μL/well was added to the cells and incubated for 1 h in dark at room temperature. In the last 10 min, the cells were stained with Hoechst stain (1 μg/mL). Post staining, cells were washed thrice with ice-cold PBS (200 μL) before capturing the image in the red channel at λ_{ex} 556 nm; λ_{em} 550 nm 615 nm.

3D culture using sodium alginate bead

For 3D culture, HepG2 cells were maintained in Dulbecco's modified Eagle's medium (DMEM, Himedia) supplemented with 10% Fetal bovine serum (FBS, Gibco). All cultures were maintained at 37°C with 5% CO_2. Then, freshly harvested from 2D cells were encapsulated in ALG beads by the method described in previous studies.[84,85] In brief, the cells (4×10^6 cells/mL alginate) were suspended in filtered sterilized 1.5% (w/v) sodium alginate solution. Then alginate solution with cells was extruded into $CaCl_2$ solution (102 mM) using a 21-gauge syringe pump. After gelation for 30 Min, alginate gel beads were washed thrice with DMEM and placed in 6 well plates with DMEM supplemented with 10% FBS at 37°C in a humidified atmosphere of under 5% CO_2 atmosphere in the air for 5 days. The medium was replaced every other day until the cell spheroids are formed.

In vitro cell viability assay of 3D cultures

The cytotoxicity effect of IITK4004 and IITK4003 on HepG2 was screened by the MTT colorimetric method.[84,85] Briefly, 3 beads/well were seeded in 96-well plates at 37°C. Then, cell scaffolds were treated with different concentrations of IITK4004 and IITK4003 (100 mM-1 nM) were added in the triplicate wells and incubated for 24 and 48 h time points. Mitomycin (10 mg/mL) was used as a positive control. After the specific times of exposure to extracts, the 3D cell spheroids were harvested from alginate beads by simply treated with Citrate buffer 55 mM/EDTA 50 mM, pH 7.4, and then resuspended in a culture medium. Then plates were centrifuged at 2000 rpm for 10 min and discarded supernatant. Then cells were incubated with a final concentration of 5 mg/mL MTT solution. After 4 h incubation, the culture medium was replaced with 100 μL of DMSO to dissolve the formazan crystals. The absorbance was read at 570/640 nm using a Tecon plate reader. The percentage of cell viability was determined, and graphs were plotted with GraphPad Prism 8.0.2.

EDX-SEM analysis

For EDS-SEM, Huh-7 cells, 3 million per T75 flask was plated and incubated standard conditions for 48 h. Then, the cells were treated with DMSO or IITK4003 and IITK4004 (20 μM of) independently for 2 h. After the treatment, cells were washed with PBS (10 mL) and scrapped in 1 mL of autoclaved water. The scraped cells were collected in a 2 mL tube and dried under vacuum (0.014 mbar) at −53°C for 6 h in a

lyophilizer (LABCONCO). From the dried sample, 0.5 mg were spread evenly on the carbon tape which was stuck over an aluminum base for gold coating under vacuum using JEOL-3000FC Auto fine coater (100 V, 40 mA, 3.5 pa) for 60 s. The gold coated samples were analyzed for the identification and quantification of iron by using Electron Probe Micro Analyser (JXA-8230, JOEL). The conditions of instrument followed to acquire the data were as follows, volts: 20 kV; process time: 60 s; dead time: 1%; count rate: 901 CPS. The data which were acquired in % mass form were plotted by using Graphpad Prism 9.0 software.

ICP-MS analysis

The dried sample prepared for EDX-SEM were also subjected to ICP-MS analysis. Here, lyophilised samples (3 mg) were digested with 1 mL of 1% HNO_3 (FINAR) and filtered through 0.2 μm syringe filter. The filtered samples were analyzed for the identification of iron levels using inductively coupled plasma mass spectrometry (ICP-MS, ThermoFisher scientific, iCAP, Qc). A standard curve was generated by using the internal standards of multi-elemental solution that majorly contain iron (0 ppb–2000 ppb). The amount of iron in the samples were estimated in ppb using the standard curve generated. The graphs were plotted by using Graphpad Prism 9.0 software. The data provided are representative of three or four independent analysis.

Synthesis of polymeric nanocarriers

Polymeric nanocarriers were prepared using a water-in-oil-in-water double emulsion method described elsewhere, previously.[64–66,86] A 10 mg amount of carboxylic acid poly (ethylene glycol)-block-poly(lactide-co-glycolide) (PLGA-b-PEG-COOH) (Sigma-Aldrich) polymer was dissolved in dichloromethane and mixed with acetonitrile solution of drugs IITK4003 or IITK4004 (1.6 mg). Thereafter, this mixture was further mixed with 100 μL of water and emulsified in an ice bath with a probe sonication for 45 s at 40% power rate. Then, 4 mL of 1.25% (w/v) sodium cholate solution dissolved in water, the biphasic mixture, was further emulsified for 3 min under similar conditions. Organic solvents were evaporated in a rotary evaporator under reduced pressure. The final volume of the nanocarrier suspension was made up to 5 mL by adding Milli-Q water. At this point the concentration of added IITK4003 was 350.6 μM and IITK4004 was 267.55μM. Free drug molecules were separated by dialysis using a dialysis tube with molecular weight cut off 2000 Da (Sigma-Aldrich) with continuous stirring for 4 h at 650 RPM.

Characterization of polymeric nanocarriers

The hydrodynamic diameter of the nanocarriers (with or without loaded drugs) were measured at 10% (v/v) dilution in water using a NanoBrook 90 Plus particle analyzer (Brookhaven Instrument).

Quantification of drug loading

The amount of loaded drug in the polymeric nanocarriers was quantified by measuring the absorbance of the drug at 380 nm for IITK4003 and 360 nm for IITK4004. Briefly, a 20 μL aliquot of drug loaded polymeric nanocarriers was diluted in 180 μL of acetonitrile and placed in an ultrasonic bath for 30 min for disassembling the nanocarriers and simultaneously releasing the drug in the organic solvent. The concentration of the released drug was interpolated through regression analysis from standard curve of absorbance vs. known concentrations of the drug.

Abbreviations

MMP: Mitochondrial membrane potential; NAC: N-acetylcysteine; Vit-E: Vitmain-E; BSO: Buthionine sulfoximine; H_2O_2: Hydrogen peroxide; ^{t}*Bu*OOH: *tert*-Butyl hydroperoxide; RPM: Rotations per minute; ROS: Reactive Oxygen Species; DCFDA: 2′,7′-Dichlorofluorescein 3′,6′-diacetate; TMRM: Tetramethyl rhodamine, methyl ester percholate; ATP: Adenosine triphosphate; SOD: Superoxide Dismutase; HRP: HorseRadish Peroxidase; DHE: Dihydroethidine; TBA: Thiobarbituric acid; MDA: Malondialdehyde; BSA: Bovine Serum Albumin; ALG beads: Alginate beads; EDTA: Ethylene diamine tetra acetic acid.; DMEM: Dulbecco's Modified Eagle Medium; FBS: Fetal Bovine Serum; PenStrep: Pencillin Streptomycin; DMSO: Dimethyl sulfoxide; CTG: CellTiter-Glo; and PBS: Phosphate Buffer Saline.

QUANTIFICATION AND STATISTICAL ANALYSIS

Data were expressed as mean ± s.d. and *p* values were calculated using an unpaired two-tailed Student's t test for pairwise comparison of variables with a 95% confidence interval and $n - 2$ degrees of freedom, where n is the total number of samples, in all Figures. Each of the biological studies were performed in two independent cell lines (Huh-7 and U2OS) and are representative of two or more independent experiments with a minimum of triple technical replicates, unless stated otherwise.